Stable and radiogenic strontium isotope fractionation during hydrothermal seawater-basalt interaction

Martin Voigt[a,*], Christopher R. Pearce[b], Andre Baldermann[c], Eric H. Oelkers[a,d]

[a] Géosciences Environnement Toulouse (GET) - CNRS, 14 avenue Édouard Belin, 31400 Toulouse, France (*correspondence: martin.voigt@get.obs-mip.fr)

[b] National Oceanography Centre Southampton, University of Southampton Waterfront Campus, European Way, Southampton SO14 3ZH, United Kingdom

[c] Institute of Applied Geosciences, Graz University of Technology, Graz, Austria

[d] Earth Sciences, UCL, Gower Street, London WC1E6BT,United Kingdom

Abstract

The fluid-rock interactions occurring in hydrothermal systems at or near mid-oceanic ridges (MOR) were studied experimentally by reacting crystalline and glassy basalt with seawater at 250 and 290 °C while monitoring the fluid phase Sr isotopic evolution ($^{87}Sr/^{86}Sr$ and $\delta^{88/86}Sr$). The results indicate that seawater Sr was incorporated into anhydrite during the early stages of seawater-basalt interaction. Fluid $^{87}Sr/^{86}Sr$ values trend towards the basaltic signature as non-stoichiometric basalt dissolution became the dominant process. This suggests that the interplay between fast Sr incorporation into secondary sulfates versus slow and continuous Sr liberation due to basalt dissolution at intermediate temperatures could partly explain previously identified discrepancies between MOR heat budget constraints and the marine $^{87}Sr/^{86}Sr$ budget. Late-stage anhydrite re-dissolution, likely caused by the fluid phase becoming more reducing through further basalt dissolution, as well as by quenching of the

experiments, represents a potential explanation for the low amounts of anhydrite found in naturally altered oceanic basalt samples. Relatively strong decreases in fluid $\delta^{88/86}$Sr values in experiments with crystalline basalt suggest that isotopically light Sr was preferentially released due to non-stoichiometric dissolution. A slight preference of anhydrite for isotopically heavy Sr ($\varepsilon^{88/86}_{\text{Anhydrite}-\text{Liquid}} = 0.33 \pm 0.020$ ‰) is indicated by the data, suggesting that changes in MOR spreading rates and Sr removal could be recorded in the isotope compositions of authigenic, sedimentary Sr phases. Such insights will help to constrain the influence of hydrothermal systems on the oceanic stable Sr cycle.

1 Introduction

Widespread hydrothermal activity at the mid-ocean ridges is well established (e.g., Stein and Stein, 1994; Alt and Teagle, 2000; Baker and German, 2004; German and Seyfried, 2014). Driven by magmatic heat associated with the generation of new crust, seawater is heated while percolating through the oceanic crust, and, after its interaction with this basaltic crust, released again to the ocean (e.g., Sleep, 1991; Bickle et al., 1998; Coogan, 2008). Fluids expelled near mid-ocean ridges, where new oceanic crust is created through submarine volcanic activity, can reach temperatures exceeding 400 °C, while further from active spreading centres, low-temperature hydrothermal fluids, driven by heat transferred from the upper mantle, are released from the crust (e.g., Elderfield and Schultz, 1996). The significance of marine hydrothermal activity on marine geochemical cycles has been widely discussed (e.g., Palmer and Edmond, 1989; Elderfield and Schultz, 1996; Mottl, 2003; Davis et al., 2003; Coogan and Dosso, 2012; German and Seyfried, 2014): high alteration temperatures near mid-ocean ridges, and the large areas and residence times of low-temperature alteration lead to chemical fluxes of similar magnitude as riverine fluxes. However, the details of chemical fluxes from these systems to the oceans, and notably the partitioning of heat transfer, fluid flow and chemical fluxes between high-temperature, near-axis hydrothermal

systems, and low-temperature off-axis venting, remain a subject of active debate (e.g., Mottl, 2003; Davis et al., 2003; Nielsen et al., 2006; German and Seyfried, 2014).

Strontium (Sr) is a particularly useful tracer of the sources and sinks of marine geochemical cycles, as the presence of both radiogenic and stable isotope systems enables different processes to be resolved (Faure and Hurley, 1963; Krabbenhöft et al., 2010; Pearce et al., 2015). For example, due to ^{87}Sr production by ^{87}Rb decay combined with the higher Rb/Sr ratios and age of the continental crust (Armstrong, 1968), the continental crust has relatively high $^{87}Sr/^{86}Sr$ ratios (where $^{87}Sr/^{86}Sr$ designates the traditional radiogenic Sr ratio corrected to a constant $^{86}Sr/^{88}Sr$ value of 0.1194; cf. Nier, 1938) compared to the unradiogenic mantle and oceanic crust. These large isotopic differences enable the use of seawater $^{87}Sr/^{86}Sr$ compositions to assess variations in marine Sr sources (Nier, 1938; Faure and Hurley, 1963). The major Sr sources to the oceans are river and groundwater discharge from the continents, which provide radiogenic $^{87}Sr/^{86}Sr$ signatures to the oceans, and marine hydrothermal fluids that have unradiogenic $^{87}Sr/^{86}Sr$ compositions derived from the basaltic oceanic crust (Davis et al., 2003; Krabbenhöft et al., 2010; Pearce et al., 2015). It has been suggested that high-temperature hydrothermal circulation is not sufficient to balance the other Sr input fluxes given the observed increase of $\sim 5.4\times10^{-5}$ Myr^{-1} (Hodell et al., 1990) in oceanic $^{87}Sr/^{86}Sr$ over the last few million years (Palmer and Edmond, 1989; Butterfield et al., 2001; Davis et al., 2003). Various explanations have been proposed to provide the missing unradiogenic $^{87}Sr/^{86}Sr$ flux, such as island arc weathering (Allègre et al., 2010; Li and Elderfield, 2013), ridge-flank hydrothermal systems (Butterfield et al., 2001), low-temperature alteration and carbonate precipitation (Coogan and Dosso, 2015), temporal variability in continental weathering (Vance et al., 2009; Krabbenhöft et al., 2010), and the dissolution of river derived basaltic particles (Jones et al., 2012b; Jones et al., 2012a; Jones et al., 2014; Jeandel and Oelkers, 2015). Furthermore, it has been suggested that variations of paleoseawater compositions significantly affected the exchange of Sr in hydrothermal systems (Antonelli et al., 2017).

77 There are, nevertheless, considerable uncertainties and debate in the magnitude of these
78 processes and fluxes, a well as the question if the marine radiogenic Sr system is presently in
79 steady state (Mokadem et al., 2015).

80 In contrast to $^{87}Sr/^{86}Sr$, stable Sr isotope ratios ($\delta^{88/86}Sr$) are affected by both mixing of
81 sources with distinct $\delta^{88/86}Sr$ values and isotopic fractionation during precipitation. At isotopic
82 steady state, the $\delta^{88/86}Sr$ composition of the marine Sr input and output fluxes should be equal.
83 However, it has been demonstrated that the $\delta^{88/86}Sr$ signature of marine carbonates (the
84 dominant Sr sink in the oceans) is significantly lower than the flux-weighted input $\delta^{88/86}Sr$
85 composition (Krabbenhöft et al., 2010; Pearce et al., 2015). This implies either an imbalance
86 in the seawater $\delta^{88/86}Sr$ (i.e. the modern system is not in isotopic steady state), and/or that the
87 $\delta^{88/86}Sr$ composition of oceanic sources and sinks, such as marine hydrothermal systems, is
88 not well quantified at present. In general, stable Sr isotopes potentially provide an additional
89 tool to resolve ambiguities arising from the $^{87}Sr/^{86}Sr$ data such the reason for increasing
90 seawater $^{87}Sr/^{86}Sr$ (e.g., changes in the riverine flux vs. its composition; Krabbenhöft et al.,
91 2010). However, persisting uncertainties and inconsistencies in both $^{87}Sr/^{86}Sr$ and $\delta^{88/86}Sr$
92 marine budgets compels further assessment of the marine Sr sources and sinks. In this context
93 the reactions occurring in seafloor hydrothermal systems are of critical importance. They are
94 thought to represent the dominant source of unradiogenic $^{87}Sr/^{86}Sr$ to seawater, yet the size of
95 this Sr flux to the oceans from high- and especially low-temperature systems remains poorly
96 quantified (Davis et al., 2003; Coogan and Dosso, 2015). Furthermore, the potential effects of
97 Sr sequestration by precipitation of secondary sulfates/carbonates in such systems on oceanic
98 $\delta^{88/86}Sr$ are currently unconstrained (Pearce et al., 2015).

99 The reactions leading to changes in the chemical composition of seawater during
100 hydrothermal alteration have been extensively studied using experimental systems (e.g.,
101 Bischoff and Dickson, 1975; Seyfried and Bischoff, 1977; Mottl and Holland, 1978; Seyfried
102 and Bischoff, 1979; Mottl et al., 1979; Seyfried and Bischoff, 1981; Seyfried and Mottl, 1982;

Seewald and Seyfried, 1990; Luhmann et al., 2017a; Luhmann et al., 2017b). Experimental constraints on the extent of isotopic fractionation during such hydrothermal reactions are, however, sparse (Menzies and Seyfried, 1979; Berndt et al., 1988; James et al., 2003). This limits the interpretation of the behaviour of isotopic tracers such as radiogenic $^{87}Sr/^{86}Sr$ ratios or $\delta^{88/86}Sr$ in natural systems and introduces significant uncertainties in marine Sr mass balance models as described above. This study was designed to overcome some of these limitations through a series of experiments reacting seawater with basaltic glass and crystalline basalt at temperatures of 250 °C and 290 °C. The interpretation of measured fluid phase Sr isotopic ratios during these experiments provides new insight into the behaviour of Sr and its isotopic ratios during seawater-basalt interaction.

2 Methods

2.1 Experimental design

Basaltic glass and crystalline basalt were reacted with seawater in 400 mL Ti-autoclaves (Fig. 1) at temperatures of 250 °C and 290 °C for 53 and 92 days, respectively. Two experiments were conducted at each temperature using either the basaltic glass or the crystalline basalt as solid starting materials (Table 1). As the autoclaves were not pressurised before heating, pressure at the experimental temperature was constrained by the liquid-gas phase relations. As pressure was not directly monitored, it was estimated approximating the seawater as a H_2O-NaCl solution with a molar NaCl fraction of 0.0106 (i.e. allocating all Cl^- to NaCl), allowing the thermodynamic equilibrium state of this H_2O-NaCl system to be predicted using the relationships in Driesner and Heinreich (2007) and Driesner (2007). Using the temperature, volume and mass constraints from our experiments, a NaCl bearing liquid phase and minor amounts of a low-NaCl vapour phase were predicted to coexist. For our experiments, pressures of 39 bar and 73 bar were calculated for the 250 °C and 290 °C experiments, respectively, which is similar to pure H_2O vapour pressures. Liquid sampling

128 during the experiments did not significantly lower the pressures in the reactors (for example,
129 pressures are predicted to drop from 73.13 bar to 72.94 bar during the 290 °C experiments),
130 but the volume changes did affect the concentration of aqueous species in some cases (see
131 section 3.1.4).

132 All reactor parts in contact with the experimental materials were constructed from Ti
133 (UT 40) with exception of a polytetrafluoroethylene (PTFE) gasket between the bottom of the
134 reactor and the closure of the autoclave (Fig. 1). Before each experiment, the autoclaves were
135 mechanically cleaned by re-machining the inner walls, filling with ultrapure water (18.2
136 MΩ×cm at 25 °C, Millipore) and heating to 200 °C for several days, then repeating this
137 procedure (including the heating of the reactor) with ~1 mol/kg bi-distilled HNO_3 and finally
138 with ultrapure water.

139 At the beginning of each experiment, the reactors were filled with basalt and seawater
140 so that the seawater to basalt mass ratio was ~10 (Table 1) consistent with previous
141 experiments and similar to conditions in submarine hydrothermal systems (Seyfried and
142 Bischoff, 1979; Seyfried and Bischoff, 1981). The mass of the reactants were lower for the
143 290 °C experiment to account for the greater thermal expansion at this temperature. Before
144 sealing the reactors, the head space was flushed with N_2 to avoid oxidation reactions caused
145 by an uptake of O_2 from the gas phase. The experiments were started by placing the reactors
146 into the furnaces, starting the rocking motion (~1 cycle/min) and heating the furnaces to the
147 desired temperature. The desired experimental temperature was reached within approximately
148 2 h in all experiments. The temperature inside the reactors was continuously monitored with a
149 type K thermocouple inserted into a thermowell in the reactors with an uncertainty of
150 approximately ± 2 °C.

151 Samples of the liquid phase in the reactors were taken during all experiments using a
152 valve with an attached water-cooling apparatus (Fig. 1). The rocking motion was stopped
153 prior to sampling and a Ti-frit, located at the sampling outlet in the reactor (pore size 5 μm),

prevented solids from leaving the autoclave. The liquid was filtered through a 0.45 µm cellulose acetate membrane at the outlet (replaced after each sampling) and collected in three separate polypropylene (PP) vials: The first ~3 mL collected during each sampling were discarded to avoid cross-contamination from the sampling device (which was cleaned using dilute bi-distilled HNO_3 and ultrapure water before and after each sampling). Subsequently, a non-acidified sample (~3 mL) was taken for pH measurements, followed by a ~15 mL sample for later compositional and isotopic analysis collected in a vial containing ~0.45 g of bi-distilled HNO_3 to avoid precipitation of solid phases due to the temperature and pressure changes after quenching of the sample.

The experiments were terminated by quenching the reactors in water so that they attained ambient temperature within approximately 30 minutes. After opening the reactors, the solid reaction products were separated from the liquid by vacuum filtration through a 0.45 µm cellulose acetate membrane, rinsed with ultrapure water, and dried at 50 °C.

2.2 Reactants

Two different types of basalt were used as reactants in the experiments: basaltic glass, and crystalline basalt (Fig. 2a, b). Both rock types were collected from a basaltic dyke on Stapafell Mountain, SW Iceland, and have been previously described by Oelkers and Gislason (2001) and Gudbrandsson et al. (2011). The chemical compositions of these samples (Table **2**) are similar to that of mid-ocean ridge basalt (MORB). Their Sr content and isotopic compositions were determined in this study, and correspond to typical basaltic values (Table 3). The crystalline basalt is composed of approximately 43 wt.% plagioclase, 47 wt.% pyroxene and 9 wt.% olivine, while only minor amounts of olivine (~3 wt.%) are present in the basaltic glass (~97 wt.% amorphous phase) according to quantitative XRD analyses. Both materials were ground using a jaw crusher and an agate disc mill before the 40-80 µm size fraction was obtained by sieving. Ultra-fine particles were removed from these powders by repeated ultrasonic cleaning in ultrapure water, followed by gravitational settling and

decantation of the supernatant water. The resulting powder was dried at 60 °C. The specific surface areas of these powders were determined to be 0.07 m^2/g and 0.4 m^2/g for the basaltic glass and crystalline basalt, respectively, by the BET technique (Brunauer et al., 1938) using Kr gas and a Quantachrome Autosorb 1-MP automated gas sorption analyser with a relative uncertainty (one standard deviation) of approximately 10%. The difference in the surface area of the two materials likely arises from differences in surface roughness, as the grain sizes are similar for both powders.

Natural seawater sampled from the equatorial Pacific Ocean from a depth of 350 m (EqPac cruise November 1992; Murray et al., 1997) was used as the initial fluid reactant for all experiments. The seawater was acidified upon collection using distilled concentrated HCl (to a pH of ~ 1.5) to prevent the precipitation of solids and growth of organic material. The pH of the seawater was re-adjusted to a natural value of ~8.14 by the gradual addition of 25 % ammonia solution (EMD Millipore Suprapur) prior to its use in the experiments (Table 4), but was not equilibrated with atmospheric CO_2 as it was filled into the reactors immediately whose headspace was subsequently flushed with N_2, so that its dissolved inorganic carbon concentrations remained low (most likely on the order of 10^{-5} to 10^{-4} mol/kg). The total ammonia and HCl concentrations were approximately 0.04 mol/kg and 0.05 mol/kg, respectively, the former potentially impacting pH evolution (cf. section 4.1).

2.3 Analytical methods

All liquid samples were analysed for their pH, elemental compositions and Sr isotopic composition. Fluid pH was measured using a Metrohm microelectrode at 22±1 °C. The electrode was calibrated against three NIST traceable pH buffer solutions (pH 4.0, 6.9 and 9.2) to achieve an analytical precision of ± 0.07 pH units based on replicate analyses of buffers and samples.

Liquid samples from the 250 °C experiments were analysed for their total Na, Mg, Si, K, Ca, Sr, and Fe contents using a ThermoFisher inductively coupled plasma atomic emission

206 spectrometer (ICP-AES), while Al contents were determined by furnace atomic adsorption
207 spectrometry (AAS) using a Perkin Elmer AAnalyst 600 (analytical uncertainties and
208 detection limits are reported in Electronic Supplementary Table 1). Concentrations of Mg, Si,
209 K, Ca, Sr, Fe and Al in the liquid samples from the experiments at 290 °C were determined by
210 inductively coupled plasma mass spectrometry (ICP-MS) using an Agilent 7500ce after
211 adding In and Re as internal standards. For these samples, Na contents were determined using
212 a Perkin Elmer AAnalyst 400 flame AAS. The seawater used as reactant was analysed by all
213 of the above mentioned techniques, and the concentrations determined by the different
214 techniques are in agreement with each other within the uncertainties. Aqueous SO_4^{2-} and Cl^- of
215 all liquid samples were determined using a Dionex ICS 2000 ion chromatography (IC)
216 system. All calibration standards were prepared from aqueous Merck Certipur solutions.
217 The $^{87}Sr/^{86}Sr$ and $\delta^{88/86}Sr$ ratios of both solid and liquid samples were determined by
218 thermal ionisation mass spectrometry (TIMS) using a ThermoFisher Triton at the National
219 Oceanography Centre, Southampton following the sample preparation and analytical
220 procedures described in Pearce et al. (2015). For each sample, an unspiked and a spiked
221 aliquot (containing an additional ^{84}Sr-^{87}Sr solution of known isotopic composition) were
222 analysed, allowing correction for mass fraction during sample preparation and analysis.
223 Radiogenic $^{87}Sr/^{86}Sr$ ratios were determined by correcting the data from the measurements of
224 the unspiked sample for instrument mass fractionation assuming the exponential mass
225 fractionation law and using an $^{86}Sr/^{88}Sr$ ratio of 0.1194. The raw mean $^{87}Sr/^{86}Sr$ ratio of NIST
226 SRM 987 during this study was 0.710251 (2 standard deviations (SD) = 7 ppm), though all
227 reported $^{87}Sr/^{86}Sr$ compositions have been corrected to an external NIST SRM 987 $^{87}Sr/^{86}Sr$
228 value of 0.710248 (McArthur et al., 2012) for comparison with published data. Over the
229 course of this study, the NIST SRM 987 standard was analysed 16 times, with 4
230 measurements at the beginning of each session with a total of 15 to 21 measurements (half of
231 these standards were processed using the same preparation methods as for the samples). No

significant drift for stable Sr isotope measurements of standards was observed over the course of these measurements, while radiogenic standard measurements decreased slightly by ~ 7 ppm towards the end of the measurements. Stable Sr isotope ratios were determined from deconvolution of the spiked and unspiked measurements using the exponential mass fractionation law and a Newton-Raphson optimisation (e.g., Ypma, 1995). The $\delta^{88/86}$Sr values, defined as $\delta^{88/86}\mathrm{Sr} \equiv \frac{\left(^{88}\mathrm{Sr}/^{86}\mathrm{Sr}\right)_{\mathrm{Sample}}}{\left(^{88}\mathrm{Sr}/^{86}\mathrm{Sr}\right)_{\mathrm{SRM987}}} - 1$ and given in units of per mil (‰, i.e. multiplied by 1000), are given relative to the mean of the repeated analyses of the NIST SRM 987 standard.

The two basalt powders used as reactants and the solid reaction products recovered from the reactors were analysed by scanning electron microscopy (SEM) using a Jeol JSM 6360LV equipped with an electron dispersive spectroscope (EDS). Powder X-ray diffraction (PXRD) patterns of the unreacted basalt powders and of the solids recovered from the reactors after the experiments were recorded on a PANalytical X'Pert PRO diffractometer (Co-Ka radiation) operated at 40 kV and 40 mA. This diffractometer is outfitted with a high-speed Scientific X'Celerator detector, 0.5° antiscattering and divergence slits, spinner stage, primary and secondary soller and automatic sample changer. The top loading technique was used for the preparation of the samples. The specimens were examined over the range 4-85° 2-θ using a step size of 0.008° 2-θ and a count time of 40 s per step. Phase identification and quantification was performed using the PANalytical X'Pert HighScore Plus software and a pdf-2 database.

2.4 Thermodynamic calculations

The saturation states (Ω) of solid phases were calculated using PHREEQC (Parkhurst and Appelo, 2013) together with its Lawrence Livermore National Laboratory (LLNL) database (Johnson et al., 2000) at the experimental temperature and saturated vapour pressure. The saturation index (SI) is defined as the base-10 logarithm of the saturation state Ω, which is the ratio of the ion activity product to the equilibrium constant of the precipitation reaction.

The enthalpy of the aqueous $MgSO_4$ complex dissociation reaction was taken from the minteq.v4 database, as it is consistent with the results of Allison et al. (1991). In these calculations, the standard state for solid phases and H_2O is the pure phase, while a hypothetical 1 mol/kg aqueous solution referenced to infinite dilution is chosen for unit activity (a) of aqueous species, both at the temperature and pressure of interest. The Livermore National Laboratory aqueous model (Daveler and Wolery, 1992), which uses the extended Debye-Hückel equation (Helgeson, 1969) was used to calculate activity coefficients of the aqueous species. As the redox state of the fluids was not specifically analysed, calculations were carried out assuming oxidising conditions (i.e. aqueous S is in the form of S^{6+}), limiting the applicability to Fe-bearing minerals. The quality of the thermodynamic database at temperatures of 200 to 300 $^{\circ}$C under seawater-like salinities is limited such that the saturation indexes calculated for the reactive fluid samples collected in this study are somewhat uncertain. For anhydrite and quartz, minerals that contain few components, the uncertainties associated with their calculated saturation indexes are likely no more than 0.2, in contrast, for feldspars and clay minerals, which have more complex hydrolysis reactions, such uncertainties likely exceed 1 (e.g., Voigt et al., in review).

2.5 Uncertainties

Unless otherwise stated, uncertainties in this study represent the 95% confidence interval (CI). The ± symbol is used to denote the half-width of the confidence interval (for normally distributed values, this corresponds to approximately 1.96 standard errors (SE)). Where possible, uncertainties were propagated through functions using linearisations. For non-algebraic or highly non-linear functions, Monte Carlo simulations were used to estimate the transformed probability distribution and the confidence interval is calculated from its quantiles (e.g., Ogilvie, 1984).

3 Results

3.1 Evolution of the reactive fluid compositions during the experiments

3.1.1 Magnesium, sulfate, calcium and potassium

The chemical composition of the fluids sampled from the reactors changed significantly during the experiments (Figs. 3 and 4, Table 4). Magnesium and SO_4^{2-} were almost completely removed from the starting seawater solution within one week of reaction with basaltic glass at both studied temperatures. This consumption was slower in the crystalline basalt experiments, such that near complete Mg removal was only achieved after three weeks at 250 °C. Calcium concentrations remained stable or decreased slightly at the beginning of the experiments, but increased during the later stages in all experiments, attaining values of approximately 42 mmol/kg (the only exception being the experiment with basaltic glass at 290 °C, where 79 mmol/kg Ca was present in the final liquid sample). The highest increases of Ca coincided with greatest Mg removal, i.e. an inverse correlation of Ca and Mg trends can be observed. Similarly to Ca, aqueous K concentrations increased during all experiments, reaching values of up to 24 mmol/kg in the 290 °C basaltic glass experiment, and approximately 17 mmol/kg in the other experiments (Table 4).

3.1.2 pH

The ambient temperature pH in the basaltic glass experiment only showed a slight decrease at 250 °C before its steady increase to approximately 9.5 at both temperatures (Figs. 3 and 4, Table 4). Conversely, the pH attained acidic values of 3.7 and 4.9 during the first month of the crystalline basalt experiments at 250 °C and 290 °C, respectively, before increasing to a final pH of approximately 9.2.

3.1.3 Strontium

After dropping during the first 24 h, aqueous Sr concentrations increased throughout the experiments, similar to the behaviour of aqueous Ca (Fig. 5, Table 4). In the basaltic glass

306 experiments, the radiogenic $^{87}Sr/^{86}Sr$ isotope ratios decreased from the initial seawater value
307 (0.709173) and attained values similar to that of the basaltic glass (0.703193) within one day.
308 This process was slower in the crystalline basalt experiment at 290 °C, where similar $^{87}Sr/^{86}Sr$
309 ratios were reached within 4 days. In the corresponding 250 °C experiment the largest
310 decrease in $^{87}Sr/^{86}Sr$ occurred between days 7 and 21, but values showed a higher variability
311 and remained above 0.704210 until the end of the experiment. During the later stages of all
312 experiments (i.e. after 1 month), the $^{87}Sr/^{86}Sr$ ratios increased slightly to final values of
313 0.704276 and 0.704114 for the basaltic glass experiments and of 0.704862 and 0.705116 for
314 the crystalline basalt experiments, respectively, at 250 and 290 °C. Stable $\delta^{88/86}Sr$ values
315 decreased from the initial seawater composition (0.38 ‰) within the first days in all
316 experiments (Fig. 5, Table 4). However, the magnitude of this change varied among the
317 experiments. In the basaltic glass experiments, $\delta^{88/86}Sr$ values similar to that of the bulk basalt
318 (0.23 ‰) were attained. Conversely, in the crystalline basalt experiments, seawater $\delta^{88/86}Sr$
319 decreased to levels significantly below that of bulk crystalline basalt (0.26 ‰) after the first
320 week. The $\delta^{88/86}Sr$ decrease was most pronounced in the 290 °C experiment, where a value of
321 -0.06 ‰ was observed temporarily. Afterwards, the $\delta^{88/86}Sr$ ratios increased steadily towards
322 the crystalline basaltic signature but always remained below this basalt value during the
323 further evolution of these experiments.

324 **3.1.4 Sodium and chloride**

325 The dissolved Na and Cl concentrations increased steadily within the first weeks and
326 more rapidly during the late stages of the experiments due to fluid sampling and related
327 formation of a low-NaCl vapour phase (see section 2.2). This interpretation is validated by the
328 composition of the quenched liquid recovered from the basaltic glass experiment at 250 °C
329 after the experiment was terminated, showing Cl^- concentrations returning to similar values as
330 those taken during the early stages of the experiment (see Table 4). Due to this process, the
331 salinity increased significantly in the last two fluid samples collected from the basaltic glass

experiment at 250 °C (≈17 % in terms of Cl^- compared to seawater, cf. Figs. 3 and 4, Table 4) and of the last samples collected from both experiments at 290 °C. No significant Cl was released from the solids in our experiments. Only small amounts of H_2O were taken up by hydrated solid alteration products; however, this process further enriches the Na and Cl concentrations in the fluids. The uptake of H_2O by the vapour phase on the Na and Cl concentration of the liquid phase was calculated using the relationships of Driesner and Heinreich (2007) and Driesner (2007), which was accounted for by the mass balance calculations and models discussed below.

3.1.5 Silica

Dissolved silica concentrations increased dramatically from the below detection quantities of the initial seawater during the first day of the experiments (Figs. 3 and 4, Table 4). At 250 °C, silica concentrations increased to 14 mmol/kg in the basaltic glass experiment and to 20 mmol/kg in the reaction with crystalline basalt, before stabilising at approximately 10 mmol/kg in both experiments. Similar trends were observed at 290 °C, but higher absolute concentrations (approximately 25 mmol/kg) were attained before a final decrease to 10 mmol/kg and 15 mmol/kg in the basaltic glass and crystalline basalt experiments, respectively.

3.1.6 Iron

The basaltic glass experiment at 250 °C reached an Fe concentration of 0.27 mmol/kg after one day before dropping to non-detectable levels, while in the corresponding experiment at 290 °C no dissolved Fe was detectable in any fluid samples (Figs. 3 and 4, Table 4). Higher Fe concentrations were reached in the experiments with crystalline basalt (2.4 mmol/kg and 4.7 mmol/kg at 250 °C and 290 °C, respectively), and concentrations above 1 mmol/kg were sustained in the lower temperature experiment for two weeks.

3.2 Solid alteration products

The solids recovered at the end of the experiments were substantially altered relative to the starting materials. The SEM images of reacted basalt from the 250 °C experiments (Fig. 2c-f) show that the initially clean and relatively smooth grain surfaces were completely covered by micrometre-scale, honeycomb-like structures typical for neo-formed smectite (e.g., Fiore et al., 2001; Baldermann et al., 2012; Baldermann et al., 2017). While the alteration features observed for the 290 °C experiments are very similar, the clayey textures seem to be more regular for both crystalline basalt experiments (Fig. 2c, d). In some cases, the formation of a protective smectite layer covering the underlying basalt grains (Fig. 2e) was observed. It seems plausible that the separation of the protective layer from the underlying basalt grain results from quenching and the sample preparation. Apart from the ubiquitous clay minerals, abundant anhydrite formed in all experiments (Fig. 2f). The size of the precipitated anhydrite crystals ranged from approximately 1 μm to 200 μm in length. A separate experiment with basaltic glass at 250 °C that was terminated after only one day showed that both of these alteration minerals were already present after this period, although the honeycomb-like smectite structures were less developed.

The formation of smectite (probably ferrous saponite) and anhydrite was confirmed by XRD analyses of the reacted basalt glass and crystalline basalt samples at both temperatures (Supplementary Fig. 1), whereas no indication for the formation of secondary carbonates such as aragonite and strontianite was found. Minor amounts of zeolite also formed during the two basaltic glass experiments, in addition to plagioclase (close to albitic composition) and serpentine minerals at 290 °C.

4 Discussion

4.1 Chemical exchange

The changes in the chemical composition of the seawater and the alteration mineral assemblage observed during the experiments in this study are comparable to those seen in natural marine hydrothermal vent fluids (e.g., German and Seyfried, 2014). Consistent with previous experimental studies (Seyfried and Bischoff, 1981; Seyfried and Mottl, 1982), Mg was found to be transferred from seawater into secondary, trioctahedral clay minerals such as saponite and serpentine that formed rapidly during the experiments, leading to the almost complete removal of Mg from the liquid (Figs. 3 and 4). Furthermore, the kinetics of Mg removal and the Ca trends at 250 °C fit are consistent with experiments at 150 °C and 300 °C reported by Seyfried and Bischoff (1979; 1981), as illustrated for the crystalline basalt experiments in Fig. 6. The rapid formation of saponite is consistent with the saturation indices for Mg-saponite calculated with PHREEQC, which indicate that the reactive liquid is extremely oversaturated with respect to this phase (Supplementary Fig. **Error! Reference source not found.**2). The formation of anhydrite consumed dissolved SO_4^{2-}, and to a lesser extent Ca, including some of the Ca released from the basalt dissolution (see section 4.2). Sodium, Cl and K are not significantly incorporated into alteration phases, with the latter being progressively enriched in the fluid. In contrast, Si and Fe released by basalt dissolution were likely scavenged by authigenic (ferrous) clay minerals (Baldermann et al., 2014; Baldermann et al., 2015; Baldermann et al., 2017) and/or in the case of Si precipitated on minor amounts of pre-existing quartz which was potentially introduced while grinding the basalt (indicated by XRD spectra; Supplementary Fig. 1) at least during the initial stage of seawater-basalt interaction (Supplementary Fig. **Error! Reference source not found.**2). The absence of Fe^{3+}-bearing clay minerals such as nontronite and Fe-O-OH phases in the reaction products (Supplementary Fig. 1) indicates that reducing conditions had been established

during the experiments, albeit traces of ferric phases (i.e. ferrihydrite or goethite), which could have been formed during quenching of the experiments. Our thermodynamic calculations also suggest that the reactive fluids were slightly undersaturated with respect to low-albite, highlighting the uncertainties inherent in current thermodynamic data at the experimental conditions as the formation of albite-rich plagioclase during the basaltic glass experiment at 290 °C is clearly indicated by XRD (cf. section 3.2).

The drop in pH observed at the beginning of the crystalline basalt experiments was predominantly caused by the incorporation of Si, Fe and Mg complexes and OH^- into the neo-formed clay minerals (Bischoff and Dickson, 1975; Seyfried and Bischoff, 1977; Seyfried and Bischoff, 1979; Seyfried and Bischoff, 1981; Seyfried and Mottl, 1982). These initially low pH are less prominent in the basaltic glass experiments, where alkaline conditions prevailed throughout the experiments (Figs. 3 and 4), because the dissolution rate of this material is faster compared to its crystalline analogue. While pH in natural hydrothermal fluids is commonly slightly acidic, which can be explained by buffering with a plagioclase-chlorite-tremolite-quartz assemblage (Seyfried et al., 2010; Pester et al., 2012), pH increased to slightly alkaline values at the end of all experiments in this study; these final pH values exceeds those seen in previous studies (Menzies and Seyfried, 1979; Seyfried and Bischoff, 1981). These high pH values are potentially related to uptake of HCl by the vapour, which is increased at high salinities (Simonson and Palmer, 1993; Palmer et al., 2004), or to the presence of low amounts of ammonium, which potentially affects pH due to its influence on aqueous speciation.

4.2 Strontium isotopic exchange

4.2.1 Initial stage (<24 hours)

The most significant Sr elemental and isotopic exchange occurred during the first 24 h. Aqueous Sr concentrations decreased by more than 70% over this time, as the $^{87}Sr/^{86}Sr$ ratio of the fluid decreased from the seawater towards the basalt value (Fig. 5). Because changes in

$^{87}Sr/^{86}Sr$ reflect the mixing between different phases and not isotopic fractionation, both the release of Sr from the basalt and the removal of Sr into alteration phases are necessary to explain these observations.

The presence of anhydrite in the solids recovered after the experiments coupled with the decrease of SO_4^{2-} during the first 24 h (Fig. 3) suggests that anhydrite was the main phase taking up Sr (Shikazono and Holland, 1983). This is consistent with the anhydrite saturation indices calculated with PHREEQC for these experiments (Supplementary Fig. **Error! Reference source not found.**2) and past observations of anhydrite precipitation when heating seawater to temperatures of 150 to 200 °C (Bischoff and Seyfried, 1978). It is worth noting, however, that the existence of minor Mg^{2+}, Ca^{2+} or Sr^{2+} in the interlayer sites of ferrous saponite is possible, because divalent cations preferentially substitute for Na^+ (Baldermann et al., 2014), although the predominance of interlayer Na^+ is likely due to the high Na concentrations (~500-600 mmol/kg, Table 4) of the reactive fluids.

Assuming that anhydrite was the only sink for aqueous Ca and SO_4^{2-} during this period, mass balance constraints allow the calculation of the mass of basalt dissolved and of anhydrite precipitated from the compositions of the initial seawater and first fluid sample, the liquid mass, and the basalt composition. Note that this calculation also assumes that the basalt dissolution was stoichiometric, which was likely not the case as inferred from Sr isotopic trends as described below. Therefore, the calculated amounts of basalt dissolved are approximate, but could be regarded as a proxy for Ca release rates if Ca release rates can be assumed to be proportional to those of Sr. The results of these calculations suggest that 4.3±0.3 g and 4.7±0.4 g of basaltic glass were dissolved at 250 °C and 290 °C, respectively, within the first day. Consistent with its aforementioned lower reactivity, only 0.62±0.06 g and 1.7±0.2 g of crystalline basalt dissolved at 250 °C and 290 °C over this time frame. The corresponding masses of anhydrite precipitated are 1.029±0.002 g and 0.85±0.02 g for the basaltic glass experiments at 250 °C and 290 °C, respectively, and 0.513±0.001 g and

455 0.74±0.02 g for the crystalline basalt experiments. The relative timing of basalt dissolution
456 and anhydrite precipitation, and the evolution of the Sr isotopic system during the initial 24 h
457 of each experiment were determined using an iterative mass balance model. In this model, the
458 mass of precipitated anhydrite ($m_{\text{Anhydrite}}$), and the fluid Sr concentration, $^{87}Sr/^{86}Sr$ and $\delta^{88/86}Sr$
459 were predicted as functions of the mass of basalt dissolved (m_{Basalt}) (see discussion below and
460 Appendix A for details). The rate of anhydrite precipitation (relative to basalt dissolution) was
461 assumed to be proportional to $(\Omega_{\text{Anhydrite}} - 1)$, where $\Omega_{\text{Anhydrite}}$ stands for the saturation state
462 of the liquid with respect to anhydrite at each model step. The amount of Sr incorporated into
463 anhydrite was calculated assuming a constant partitioning coefficient between Sr in anhydrite
464 and liquid $D_{\text{Sr}} = (\mathrm{d}m^{\text{Sr}}_{\text{Anhydrite}}/\mathrm{d}m^{\text{Ca}}_{\text{Anhydrite}})/(m^{\text{Sr}}_{\text{Liquid}}/m^{\text{Ca}}_{\text{Liquid}})$ for each experiment, where m^i_p
465 denotes the mass of element i in phase p. The best-fit values for D_{Sr} range from 0.56 to 0.84,
466 which is similar to the range of experimentally determined values of 0.27 to 0.73 (Shikazono
467 and Holland, 1983) and partition coefficients of 0.60 (2 s.d. = 0.28) derived from the TAG
468 hydrothermal mound (Teagle et al., 1998a). It should be noted, however, that partitioning of
469 Sr between fluid and anhydrite is potentially affected by kinetic effects due to the fast
470 precipitation in our experiments: it is well established that non-equilibrium partitioning can
471 lead to significant variability in partitioning coefficients (e.g., DePaolo, 2011), suggesting that
472 they might be different in natural hydrothermal systems, where anhydrite precipitation is
473 likely slower in most cases. The stable Sr isotopic evolution was constrained by two
474 fractionation factors, defined as

$$\alpha^{88/86}_{\text{Anhydrite}-\text{Liquid}} \equiv \frac{\mathrm{d}^{88}\text{Sr}_{\text{Anhydrite}}/\mathrm{d}^{86}\text{Sr}_{\text{Anhydrite}}}{^{88}\text{Sr}_{\text{Liquid}}/^{86}\text{Sr}_{\text{Liquid}}} \quad (4.1)$$

475 and

$$\alpha^{88/86}_{\text{CrytBasalt-Liquid}} \equiv \frac{^{88}\text{Sr}_{\text{CrystBasalt}}/^{86}\text{Sr}_{\text{CrystBasalt}}}{\mathrm{d}^{88}\text{Sr}_{\text{Liquid}}/\mathrm{d}^{86}\text{Sr}_{\text{Liquid}}} \quad (4.2)$$

where $^{A}Sr_{p}$ stands for the amount of the Sr isotope with mass number A in phase p. The use of the differentials (d) signifies that isotopic fractionation was assumed to be irreversible. The latter factor, describing Sr isotopic fractionation between dissolving crystalline basalt (dSr_{Liquid}) and the bulk crystalline basalt ($Sr_{CrystBasalt}$) was introduced, to account for the systematically larger $\delta^{88/86}$Sr variations in the experiments with crystalline basalt compared to basaltic glass (Fig. 5). This apparent fractionation is likely the result of the preferential dissolution of minerals having a stable Sr composition distinct from that of the bulk basalt. The effect of non-stoichiometric dissolution has also been suggested to explain stable Sr isotopic signatures in continental weathering environments (Halicz et al., 2008; Wei et al., 2013). The model was applied to all four experiments simultaneously to obtain the best-fit values for unknown parameters (D_{Sr}, $\alpha_{i,\ ...}$), but distinct values of these parameters for different experiments or temperatures were allowed as described above and in Appendix A.

Model predictions are shown in Fig. 7 and Fig. 8, and reveal a good fit to the experimental data. Accordingly, fast anhydrite precipitation (compared to basalt dissolution) from seawater is predicted at the experimental temperatures (Bischoff and Seyfried, 1978), leading to a drop in aqueous Sr concentrations, while $^{87}Sr/^{86}Sr$ remains relatively constant at this early stage. Subsequently, basalt dissolution becomes the dominant process and fluid $^{87}Sr/^{86}Sr$ decreases towards the basalt signature, which is promoted by the lower Sr content of the fluid. Afterwards, aqueous Sr concentrations remain stable or increase slightly due to ongoing basalt dissolution (Fig. 8). At this stage, anhydrite precipitation is limited by the low SO_4^{2-} concentrations in the fluids while $^{87}Sr/^{86}Sr$ remain low (Fig. 8). This result is similar to the proposed reaction path of Berndt et al. (1988), and consistent with the trends inferred from anhydrite found in altered basalts from the Costa Rica Rift, eastern Pacific (ODP Hole 504B, Teagle et al., 1998b), while evidence for the last stage of fluid evolution was missing in these natural anhydrite samples.

501 The model results further suggest that changes in aqueous $\delta^{88/86}$Sr are caused by
502 isotopic fractionation between the reactive fluid and the precipitating anhydrite, as well as by
503 the non-stoichiometric dissolution of crystalline basalt. The best-fit anhydrite-liquid
504 fractionation factor is $\varepsilon^{88/86}_{\text{Anhydrite}-\text{Liquid}} = (\alpha^{88/86}_{\text{Anhydrite}-\text{Liquid}} - 1) = 0.034 \pm 0.019$ ‰. This
505 value is slightly positive suggesting that anhydrite preferentially incorporates heavier Sr
506 isotopes. The $\varepsilon^{88/86}_{\text{CrystBasalt-Liquid}}$ values are 0.27±0.17 ‰ and 0.34±0.03 ‰ at 250 °C and
507 290 °C, respectively (Fig. 9) suggesting that the light Sr isotopes are preferentially released
508 during non-stoichiometric crystalline basalt dissolution. This can also be seen from the
509 changes in fluid Sr concentration and $\delta^{88/86}$Sr in the experiment with crystalline basalt at
510 290 °C between samples 01 and 02 (Fig. 5): Strontium concentrations increase from very low
511 levels to 37 µmol/kg, indicating that almost all Sr in fluid sample 02 originates from the
512 dissolving basalt, because anhydrite re-dissolution is unlikely at this point as $^{87}Sr/^{86}Sr$
513 remained low. Therefore, the difference in $\delta^{88/86}$Sr of sample 02 and the bulk crystalline
514 basalt, approximately 0.18 ‰, is likely attributable to the fractionation of Sr during crystalline
515 basalt dissolution; this fractionation is of similar magnitude as the fractionation factors
516 obtained by the mass balance model. Fig. 9 shows that the uncertainties of modelled
517 $\varepsilon^{88/86}_{\text{Anhydrite}-\text{Liquid}}$ and $\varepsilon^{88/86}_{\text{CrystBasalt-Liquid}}$ are inversely correlated, so that if a lower degree of
518 fractionation during non-stoichiometric crystalline basalt dissolution in our experiments could
519 be inferred from independent constraints, the best fit $\varepsilon^{88/86}_{\text{Anhydrite}-\text{Liquid}}$ would increase.
520 It should be noted that the primary incentive of this mass balance model is to explain the
521 variation of Sr concentrations and isotopic composition in the fluid samples of the
522 experiments in this study and to extract isotopic fractionation factors from these data. While
523 the general trends seen here are likely to occur in natural marine hydrothermal systems as
524 well, a quantitative, predictive model of Sr isotope variations in such systems is beyond the

scope of this model (e.g. due to differences in rates of anhydrite precipitation as explained above).

4.2.2 Sr evolution at elapsed times >24 hours

Following the initial period of coupled anhydrite precipitation and basalt dissolution, the Sr concentrations in the fluid phase increased. Aqueous $^{87}Sr/^{86}Sr$ also increased slightly during the later stages of all experiments (Fig. 5 and solid lines in Fig. 8), this suggest this evolution is not driven by basalt dissolution, as this would be expected to drive aqueous $^{87}Sr/^{86}Sr$ towards the lower basalt signature. Since this phenomenon also occurs in the basaltic glass experiments (which is assumed to have a homogeneous $^{87}Sr/^{86}Sr$ composition), the dissolution of a primary mineral with elevated $^{87}Sr/^{86}Sr$ compared to the bulk basalt is unlikely to be the cause of this process. It seems likely, therefore, that the increase in $^{87}Sr/^{86}Sr$ is driven by the dissolution of previously precipitated alteration minerals that incorporated the higher $^{87}Sr/^{86}Sr$ ratios of the initial seawater. Note that the degree of supersaturation with respect to anhydrite calculated with PHREEQC decreased during all experiments, and undersaturation was predicted for some of the later fluid samples in the crystalline basalt experiments (Supplementary Fig. **Error! Reference source not found.**2). Assuming a mean $^{87}Sr/^{86}Sr$ ratio of 0.708938 for the precipitated anhydrite (as estimated by the mass balance model described earlier), mass balance calculations suggest that up to 15 % of the anhydrite may have been re-dissolved. Since SO_4^{2-} did not increase significantly during the later stages of the experiments (Fig. 3), a possible mechanism for anhydrite re-dissolution is the reduction of aqueous SO_4^{2-} by the oxidation of Fe^{2+} released by basalt dissolution, leading to an undersaturation with respect to anhydrite and its subsequent re-dissolution. Although the reduced aqueous S concentrations are not available for our experiments (and PHREEQC saturation states in this study were calculated assuming that sulfur is present as S^{6+}), calculations by Mottl et al. (1979) under similar conditions suggest that anhydrite became metastable during their experimental runs due to the reducing nature of the final fluids.

551 Furthermore, it is possible that the fast precipitation of anhydrite at the beginning of the
552 experiments lead to the incorporation of higher amounts of Sr than at equilibrium due to
553 kinetic effects, so that Sr was released from anhydrite during the later stages due to its re-
554 crystallization (Syverson et al., 2016; Scheuermann et al., 2018), contributing to the release of
555 radiogenic Sr.

556 Reactive fluid $\delta^{88/86}$Sr remained relatively constant after the early anhydrite
557 precipitation (Fig. 5) with the exception of the crystalline basalt experiment at 290 °C, where
558 the extremely low aqueous $\delta^{88/86}$Sr gradually increase towards the basaltic $\delta^{88/86}$Sr value,
559 likely due to continued basalt dissolution and/or possible anhydrite re-dissolution.

560 ## 4.3 Implications for the marine Sr budget

561 The contribution of hydrothermal systems to the marine $^{87}Sr/^{86}Sr$ budget can be
562 estimated by comparing the heat budget of mid-ocean ridges with the cooling of new oceanic
563 lithosphere. Estimates of the latent heat of crystallisation and the required amount of cooling
564 of newly created oceanic crust places upper limits on the amount of heat transferred to the
565 oceans through hydrothermal circulation at mid ocean-ridges. Assuming a certain distribution
566 of fluid temperatures, the corresponding hydrothermal water flux can be calculated (Morton
567 and Sleep, 1985; Palmer and Edmond, 1989; Elderfield and Schultz, 1996; Mottl, 2003; Davis
568 et al., 2003). This, in turn, allows estimation of the contribution of these hydrothermal
569 systems to the marine $^{87}Sr/^{86}Sr$ budget, assuming the change of $^{87}Sr/^{86}Sr$ and Sr concentration
570 in the seawater during hydrothermal alteration is known. Based on such calculations, Davis et
571 al. (2003) estimated that high-temperature fluids (400 °C), transferring 50 % of the available
572 heat and cooling the lower crust to 860 °C, can only supply $1/6^{th}$ of the unradiogenic Sr
573 required to balance the other marine Sr fluxes (mainly the high-$^{87}Sr/^{86}Sr$ river input). Our
574 results show that fluids with low $^{87}Sr/^{86}Sr$ ratios and Sr concentrations comparable to that of
575 seawater can be generated by seawater-basalt interactions at 250 °C within 2 months, and
576 even faster at 290 °C. This is consistent with the experimental data of James et al. (2003),

577 who observed significant Sr exchange with basalt even at 150 °C. The time required for Sr
578 exchange in our experiments is well within the residence time of ≤ 3 years estimated for fluids
579 with temperatures of above 200 °C in the Juan de Fuca Ridge hydrothermal system by Kadko
580 and Butterfield (1998) using Ra isotopes. It is also within the range of residence times on the
581 order of years estimated independently by Fisher (2003). Assuming, as an example and upper
582 limit, that the 50 % of the available heat not removed by high-temperature (400 °C) fluids in
583 the Davis et al. (2003) estimate is lost through intermediate-temperature (250 °C) fluids, the
584 calculated basaltic Sr flux to the oceans increases by a factor of ~3.2, reducing the missing
585 basaltic Sr flux in the marine $^{87}Sr/^{86}Sr$ budget by half. This scenario assumes that such
586 intermediate-temperature fluids interact with basalts of relatively unradiogenic (i.e. unaltered)
587 Sr composition, which is likely as alteration at lower temperatures in the ridge flanks is
588 concentrated in the volcanic section, where higher-temperature circulation focuses on the
589 underlying sheeted dikes and gabbros (e.g., Staudigel, 2014). The large uncertainties in both
590 the amount of heat transferred from the crust to the oceans and the partitioning of
591 hydrothermal fluid temperatures (German and Seyfried, 2014) limit a more detailed
592 estimation of the basaltic Sr flux from hydrothermal systems. However, their potential to help
593 reconcile the marine $^{87}Sr/^{86}Sr$ budget means that intermediate-temperature hydrothermal
594 fluids could play a significant role in the global heat flux at MORs, supporting a similar
595 notion of Nielsen et al. (2006), and complementing other proposed unradiogenic $^{87}Sr/^{86}Sr$
596 sources such as island arc weathering (Allègre et al., 2010), low-temperature alteration and
597 carbonate precipitation (Coogan and Dosso, 2015) and dissolution of river derived basaltic
598 particles (Jones et al., 2012a).

599 Apart from heat flux constraints discussed above, Davis et al. (2003) noted that the
600 extent of ocean crust alteration is inconsistent with the current marine $^{87}Sr/^{86}Sr$ budget. This
601 argument is based on the assumption that basalt alteration occurs solely by Sr isotopic
602 exchange with the fluids, replacing the low MORB $^{87}Sr/^{86}Sr$ by high seawater $^{87}Sr/^{86}Sr$ while

603 leaving the Sr concentrations unchanged. Our experimental results and Sr isotopic modelling
604 indicate that isotopic exchange occurs mainly during the early anhydrite precipitation and
605 subsequent release of unradiogenic $^{87}Sr/^{86}Sr$ by basalt dissolution. If anhydrite is re-dissolved
606 at a later stage, the $^{87}Sr/^{86}Sr$ composition of the altered basalt may be similar to the fresh
607 basalt, such that the $^{87}Sr/^{86}Sr$ ratios of the recovered altered oceanic rocks (e.g., Staudigel et
608 al., 1995; Alt and Teagle, 2000; Harris et al., 2015) may not accurately reflect the degree of
609 isotopic Sr exchange. In the present experiments, re-dissolution of anhydrite was most likely
610 caused by the establishment of reducing conditions due to the release of Fe^{2+} (cf. section
611 4.2.2). Furthermore, increased SO_4^{2-} in the quenched liquid compared to the final sample
612 taken at experimental temperature (Table 4) indicates that anhydrite rapidly re-dissolves when
613 it becomes undersaturated at lower temperatures (as the solubility of anhydrite is retrograde).
614 In natural systems, anhydrite re-dissolution might occur due to interactions with circulating
615 low-temperature fluids at a later time (Mottl et al., 1979). Such processes limit the use of
616 altered basalt compositions to infer the hydrothermal Sr flux to the oceans and provide a
617 potential explanation for the Sr imbalances arising from models such as the marine Sr budget
618 calculations of Davis et al. (2003) and the global oceanic high-temperature hydrothermal
619 chemical exchange model of Coogan and Dosso (2012). It should also be noted that anhydrite
620 has been found where expected in undisturbed oceanic crustal sections that have been
621 sampled, but that there is a lack of samples from undisturbed basement sites (Alt, 2003).
622 Similar to the radiogenic $^{87}Sr/^{86}Sr$ imbalance in the marine budget, several studies
623 reported a disequilibrium between marine Sr input and output fluxes by analysing stable
624 $\delta^{88/86}Sr$ budgets (Krabbenhöft et al., 2010; Pearce et al., 2015). In these studies, the estimated
625 $\delta^{88/86}Sr$ of the combined marine Sr inputs, dominated by rivers and hydrothermal systems
626 (~0.3 ‰), is significantly heavier than the carbonate sink (0.15 to 0.21 ‰), suggesting that
627 seawater $\delta^{88/86}Sr$ is currently not at steady state. However, only a few $\delta^{88/86}Sr$ data of
628 hydrothermal fluids are available at present, with Pearce et al. (2015) deriving a value of

629 $\delta^{88/86}$Sr=0.24 ‰ by extrapolation of eleven hydrothermal fluid measurements to a MORB
630 hydrothermal endmember composition. Our experiments suggest that significantly lighter
631 fluid $\delta^{88/86}$Sr compositions may be reached in reactions with crystalline basalt. Although there
632 is no requirement for modern seawater $\delta^{88/86}$Sr to be at steady state (and indeed, glacial-
633 interglacial weathering effects would imply that this is unlikely to be the case; Vance et al.,
634 2009), a lower integrated hydrothermal $\delta^{88/86}$Sr composition, or a larger net flux of this
635 composition, would shift the combined marine input $\delta^{88/86}$Sr towards lighter values, reducing
636 the suggested imbalance between current input and output fluxes. Furthermore, as Sr is
637 incorporated into anhydrite during precipitation from temperate seawater, hydrothermal
638 systems may also represent an important but currently overlooked Sr sink in the marine Sr
639 cycle. The relatively small $\delta^{88/86}$Sr isotopic fractionation between anhydrite and liquid
640 observed during the early stage of hydrothermal alteration in our experiments produces a
641 $\delta^{88/86}$Sr composition similar to that of seawater. Therefore, marine hydrothermal systems may
642 shift the flux-weighted $\delta^{88/86}$Sr output composition towards heavier values, further reducing
643 the potential imbalance between global Sr sources and sinks. However, the global significance
644 of hydrothermal sinks relative to the large carbonate burial Sr flux (Krabbenhöft et al., 2010;
645 Pearce et al., 2015) is not well constrained at present.

646 Importantly, the possibility that hydrothermal fluid $\delta^{88/86}$Sr compositions may be
647 isotopically lighter than previously inferred provides new insight into the processes that
648 govern marine Sr exchange, including its fractionation during incorporation into anhydrite
649 and non-stoichiometric basalt dissolution. The resulting lower hydrothermal $\delta^{88/86}$Sr input flux
650 would also affect models of past seawater $\delta^{88/86}$Sr, and therefore put further constraints on
651 past oceanic carbonate fluxes as aragonite and calcite can take up significant amounts of Sr
652 (Vollstaedt et al., 2014). Furthermore, the magnitude of isotopic fractionation at equilibrium
653 increases with decreasing temperature (Urey, 1947; Bigeleisen and Mayer, 1947), so that Sr
654 isotopic fractionation between anhydrite and liquid may likely be larger in low-temperature

655 systems, unless equilibrium fractionation is cancelled out by opposing kinetic isotope effects.
656 On the other hand, isotopic fraction is likely smaller at higher temperatures (> 400 °C),
657 suggesting that $\delta^{88/86}$Sr potentially provides a tool to distinguish high- vs. low-temperature Sr
658 exchange in altered samples from the oceanic crust: while mass balances yield Sr isotopic
659 compositions of the bulk solids at the end of the experiments ranging in $^{87}Sr/^{86}Sr$ from
660 0.705706 to 0.706541, which is similar to values of natural samples at varying temperatures,
661 mass balances indicate $\delta^{88/86}$Sr of 0.28 ‰ and 0.29 ‰ for the final solids of experiments with
662 basaltic glass at 250 and 290 °C, respectively, and 0.35 ‰ and 0.37 ‰ for the corresponding
663 experiments with crystalline basalt. This indicates that basalt altered at moderate temperatures
664 may be significantly heavier compared to fresh basalt ($\delta^{88/86}$Sr of 0.23-0.26 ‰), which is
665 unlikely to occur at higher temperatures due to smaller magnitudes of fractionation.
666

667 # 5 Conclusions

668 Basaltic glass and crystalline basalt were reacted with seawater at 250 °C and 290 °C
669 and at saturated vapour pressure. Chemical exchange was monitored by liquid phase
670 sampling, and the results agree well with those obtained from direct measurements of mid-
671 ocean ridge vent fluid compositions. Minor differences, such as an increase of pH after near
672 complete removal of aqueous Mg by authigenic ferrous saponite and serpentine, may be
673 related to the absence of epidote from the alteration mineral assemblage.

674 The Sr concentration, radiogenic $^{87}Sr/^{86}Sr$ ratio and stable $\delta^{88/86}$Sr composition of the
675 fluid phase changed considerably during the experiments. An initial drop in $^{87}Sr/^{86}Sr$ towards
676 basaltic values coupled with a decrease in Sr concentrations can be modelled by assuming Sr
677 removal via anhydrite precipitation, followed by an increased influence of Sr release from
678 basalt dissolution over time as the liquid becomes depleted in SO_4^{2-}. A decrease in $\delta^{88/86}$Sr
679 observed during the early stage of basalt-seawater interaction suggests that isotopically light

680 Sr may be preferentially released during non-stoichiometric crystalline basalt dissolution. In
681 contrast, anhydrite shows a slight preference for isotopically heavy Sr with $\varepsilon^{88/86}_{\text{Anhydrite-Liquid}} =$
682 0.034 ± 0.019 ‰. The later evolution of the Sr isotopic composition of the fluids suggests
683 that up to 15 % of the precipitated anhydrite was re-dissolved, potentially resulting from
684 reducing conditions and quenching of the fluids at the end of the experiments.

685 Given the rapid achievement of near basaltic $^{87}Sr/^{86}Sr$ signatures and significant
686 changes in the Sr concentrations even at 250 °C, intermediate-temperature oceanic
687 hydrothermal fluids could be the source of some of the 'missing basaltic Sr input' that has
688 been postulated in marine radiogenic Sr budgets (e.g., Davis et al., 2003). Furthermore, the
689 inconsistency of observed MORB alteration patterns with the marine Sr budget and low
690 amounts of anhydrite found in ocean crust profiles (Teagle et al., 1998b) may be related to the
691 re-dissolution of anhydrite induced during later circulation of reducing or low-temperature
692 fluids. However, the persisting uncertainties in the temperature distribution of the global
693 hydrothermal water flux complicate the quantitative balancing of the marine Sr budget, which
694 should also include other proposed low-$^{87}Sr/^{86}Sr$ sources such as island arc weathering
695 (Allègre et al., 2010), dissolution of riverine particulate materials (Jones et al., 2012a) and
696 low-temperature alteration and carbonate precipitation (Coogan and Dosso, 2015).

697 Finally, our experimental data suggests that marine hydrothermal fluids with an
698 isotopically light $\delta^{88/86}Sr$ signature can be generated by isotopic fractionation during both
699 anhydrite precipitation and non-stoichiometric crystalline basalt dissolution. Such insights
700 into the processes that potentially affect seawater $\delta^{88/86}Sr$ highlight the need for detailed data
701 on the $\delta^{88/86}Sr$ of the marine hydrothermal outputs, which will help to further constrain models
702 of the current and past marine Sr cycle (Krabbenhöft et al., 2010; Vollstaedt et al., 2014;
703 Pearce et al., 2015) and thus its relationship to global changes in plate tectonics, weathering,
704 and climate.

Acknowledgements

This research was supported by the CO2-REACT Marie Curie Actions Initial Training Network which was funded by the European Union. The authors would like to thank Frederic Candaudap, Aurélie Marquet, Alain Castillo, Pascal Gisquet, Thierry Aigouy, Stephanie Mounic, Mathieu Benoit, Carole Causserand, Manuel Henry, Jonathan Prunier, Matt Cooper, and Agnes Michalik for help with analyses and technical assistance. We would also like to thank Deirdre Clark, Jan Přikryl, and Sigurður Reynir Gíslason for providing the Stapafell basalt, as well as Catherine Jeandel for providing the seawater. Reviews by Nicholas Pester, Sune Nielsen, and an anonymous reviewer were greatly appreciated by the authors, and we thank Jeffrey Alt for editorial handling of the manuscript.

References

Allègre C. J., Louvat P., Gaillardet J., Meynadier L., Rad S. and Capmas F. (2010) The fundamental role of island arc weathering in the oceanic Sr isotope budget. *Earth Planet. Sci. Lett.* **292**, 51–56.

Allison J. D., Brown D. S. and Novo-Gradac K. J. (1991) *MINTEQA2/PRODEFA2 - A geochemical assessment model for environmental systems: Version 3.0 User's Manual*., Environmental Research Laboratory, Office of Research and Development, U.S. Environmental Protection Agency, Athens, Georgia.

Alt J. C. (2003) Hydrothermal fluxes at mid-ocean ridges and on ridge flanks. *Comptes Rendus Geosci.* **335**, 853–864.

Alt J. C. and Teagle D. A. (2000) Hydrothermal alteration and fluid fluxes in ophiolites and oceanic crust. In *Ophiolites and oceanic crust: new insights from field studies and the Ocean Drilling Program* (eds. Y. Dilek, E. M. Moores, D. Elthon, and A. Nicolas). Geological Society of America Special Paper. Boulder, Colorado. pp. 273–282.

Antonelli M. A., Pester N. J., Brown S. T. and DePaolo D. J. (2017) Effect of paleoseawater composition on hydrothermal exchange in midocean ridges. *Proc. Natl. Acad. Sci.* **114**, 12413–12418.

Armstrong R. L. (1968) A model for the evolution of strontium and lead isotopes in a dynamic Earth. *Rev. Geophys.* **6**, 175–199.

Baker E. T. and German Christopher R. (2004) On the global distribution of hydrothermal vent fields. In *Mid-ocean ridges* (eds. C. R. German, J. Lin, and L. M. Parson). Geophysical Monograph Series. American Geophysical Union, Washington, D. C. pp. 245–266.

738 Baldermann A., Dietzel M., Mavromatis V., Mittermayr F., Warr L. N. and Wemmer K.
739 (2017) The role of Fe on the formation and diagenesis of interstratified glauconite-
740 smectite and illite-smectite: A case study of Lower Cretaceous shallow-water
741 carbonates. *Chem. Geol.* **453**, 21–34.

742 Baldermann A., Dohrmann R., Kaufhold S., Nickel C., Letofsky-Papst I. and Dietzel M.
743 (2014) The Fe-Mg-saponite solid solution series a hydrothermal synthesis study. *Clay*
744 *Miner.* **49**, 391–415.

745 Baldermann A., Grathoff G. H. and Nickel C. (2012) Micromilieu-controlled glauconitization
746 in fecal pellets at Oker (Central Germany). *Clay Miner.* **47**, 513–538.

747 Baldermann A., Warr L. N., Letofsky-Papst I. and Mavromatis V. (2015) Substantial iron
748 sequestration during green-clay authigenesis in modern deep-sea sediments. *Nat.*
749 *Geosci.* **8**, 885–889.

750 Berndt M. E., Seyfried W. E. Jr. and Beck J. W. (1988) Hydrothermal alteration processes at
751 midocean ridges: Experimental and theoretical constraints from Ca and Sr exchange
752 reactions and Sr isotopic ratios. *J. Geophys. Res. Solid Earth* **93**, 4573–4583.

753 Bickle M. J., Teagle D. A. H., Beynon J. and Chapman H. J. (1998) The structure and controls
754 on fluid-rock interactions in ocean ridge hydrothermal systems: constraints from the
755 Troodos ophiolite. *Geol. Soc. Lond. Spec. Publ.* **148**, 127–152.

756 Bigeleisen J. and Mayer M. G. (1947) Calculation of equilibrium constants for isotopic
757 exchange reactions. *J. Chem. Phys.* **15**, 261–267.

758 Bischoff J. L. and Dickson F. W. (1975) Seawater-basalt interaction at 200°C and 500 bars:
759 Implications for origin of sea-floor heavy-metal deposits and regulation of seawater
760 chemistry. *Earth Planet. Sci. Lett.* **25**, 385–397.

761 Bischoff J. L. and Seyfried W. E. Jr. (1978) Hydrothermal chemistry of seawater from 25 ° to
762 350°C. *Am. J. Sci.* **278**, 838–860.

763 Brunauer S., Emmett P. H. and Teller E. (1938) Adsorption of gases in multimolecular layers.
764 *J. Am. Chem. Soc.* **60**, 309–319.

765 Butterfield D. A., Nelson B. K., Wheat C. G., Mottl M. J. and Roe K. K. (2001) Evidence for
766 basaltic Sr in midocean ridge-flank hydrothermal systems and implications for the
767 global oceanic Sr isotope balance. *Geochim. Cosmochim. Acta* **65**, 4141–4153.

768 Charlton S. R. and Parkhurst D. L. (2011) Modules based on the geochemical model
769 PHREEQC for use in scripting and programming languages. *Comput. Geosci.* **37**,
770 1653–1663.

771 Coogan L. A. (2008) Reconciling temperatures of metamorphism, fluid fluxes, and heat
772 transport in the upper crust at intermediate to fast spreading mid-ocean ridges.
773 *Geochem. Geophys. Geosystems* **9**, Q02013.

774 Coogan L. A. and Dosso S. (2012) An internally consistent, probabilistic, determination of
775 ridge-axis hydrothermal fluxes from basalt-hosted systems. *Earth Planet. Sci. Lett.*
776 **323–324**, 92–101.

Coogan L. A. and Dosso S. E. (2015) Alteration of ocean crust provides a strong temperature dependent feedback on the geological carbon cycle and is a primary driver of the Sr-isotopic composition of seawater. *Earth Planet. Sci. Lett.* **415**, 38–46.

Daveler S. A. and Wolery T. J. (1992) *EQPT, a data file preprocessor for the EQ3/6 software package: User's guide and related documentation (version 7.0)*., Lawrence Livermore National Laboratory, Livermore, California.

Davis A. C., Bickle M. J. and Teagle D. A. H. (2003) Imbalance in the oceanic strontium budget. *Earth Planet. Sci. Lett.* **211**, 173–187.

DePaolo D. J. (2011) Surface kinetic model for isotopic and trace element fractionation during precipitation of calcite from aqueous solutions. *Geochim. Cosmochim. Acta* **75**, 1039–1056.

Driesner T. (2007) The system H_2O–NaCl. Part II: Correlations for molar volume, enthalpy, and isobaric heat capacity from 0 to 1000 °C, 1 to 5000 bar, and 0 to 1 X_{NaCl}. *Geochim. Cosmochim. Acta* **71**, 4902–4919.

Driesner T. and Heinrich C. A. (2007) The system H_2O–NaCl. Part I: Correlation formulae for phase relations in temperature–pressure–composition space from 0 to 1000 °C, 0 to 5000 bar, and 0 to 1 X_{NaCl}. *Geochim. Cosmochim. Acta* **71**, 4880–4901.

Elderfield H. and Schultz A. (1996) Mid-ocean ridge hydrothermal fluxes and the chemical composition of the ocean. *Annu. Rev. Earth Planet. Sci.* **24**, 191–224.

Faure G. and Hurley P. M. (1963) The isotopic composition of strontium in oceanic and continental basalts: Application to the origin of igneous rocks. *J. Petrol.* **4**, 31–50.

Fiore S., Huertas F. J., Huertas F. and Linares J. (2001) Smectite formation in rhyolitic obsidian as inferred by microscopic (SEM-TEM-AEM) investigation. *Clay Miner.* **36**, 489–500.

Fisher A. T. (2003) Geophysical constraints on hydrothermal circulation observations and models. In *Energy and mass transfer in marine hydrothermal systems* (eds. P. E. Halbach, V. Tunnicliffe, and J. R. Hein). Dahlem University Press, Berlin, Germany. pp. 29–52.

German C. R. and Seyfried W. E. Jr. (2014) Hydrothermal processes. In *Treatise on geochemistry* (ed. K. K. Turekian). Elsevier, Oxford, England. pp. 191–233.

Gudbrandsson S., Wolff-Boenisch D., Gíslason S. R. and Oelkers E. H. (2011) An experimental study of crystalline basalt dissolution from $2 \leqslant pH \leqslant 11$ and temperatures from 5 to 75°C. *Geochim. Cosmochim. Acta* **75**, 5496–5509.

Halicz L., Segal I., Fruchter N., Stein M. and Lazar B. (2008) Strontium stable isotopes fractionate in the soil environments? *Earth Planet. Sci. Lett.* **272**, 406–411.

Harris M., Coggon R. M., Smith-Duque C. E., Cooper M. J., Milton J. A. and Teagle D. A. H. (2015) Channelling of hydrothermal fluids during the accretion and evolution of the upper oceanic crust: Sr isotope evidence from ODP Hole 1256D. *Earth Planet. Sci. Lett.* **416**, 56–66.

Helgeson H. C. (1969) Thermodynamics of hydrothermal systems at elevated temperatures and pressures. *Am. J. Sci.* **267**, 729–804.

Hodell D. A., Mead G. A. and Mueller P. A. (1990) Variation in the strontium isotopic composition of seawater (8 Ma to present) : Implications for chemical weathering rates and dissolved fluxes to the oceans. *Chem. Geol. Isot. Geosci. Sect.* **80**, 291–307.

James R. H., Allen D. E. and Seyfried W. E. Jr. (2003) An experimental study of alteration of oceanic crust and terrigenous sediments at moderate temperatures (51 to 350°C): insights as to chemical processes in near-shore ridge-flank hydrothermal systems. *Geochim. Cosmochim. Acta* **67**, 681–691.

Jeandel C. and Oelkers E. H. (2015) The influence of terrigenous particulate material dissolution on ocean chemistry and global element cycles. *Chem. Geol.* **395**, 50–66.

Johnson J., Anderson G. and Parkhurst D. (2000) *Database thermo.com.V8.R6.230.*, Lawrence Livermore Natational Laboratory, Livermore, California, USA.

Jones M. T., Gislason S. R., Burton K. W., Pearce C. R., Mavromatis V., von Strandmann P. A. P. and Oelkers E. H. (2014) Quantifying the impact of riverine particulate dissolution in seawater on ocean chemistry. *Earth Planet. Sci. Lett.* **395**, 91–100.

Jones M. T., Pearce C. R., Jeandel C., Gíslason S. R., Eiriksdottir E. S., Mavromatis V. and Oelkers E. H. (2012a) Riverine particulate material dissolution as a significant flux of strontium to the oceans. *Earth Planet. Sci. Lett.* **355–356**, 51–59.

Jones M. T., Pearce C. R. and Oelkers E. H. (2012b) An experimental study of the interaction of basaltic riverine particulate material and seawater. *Geochim. Cosmochim. Acta* **77**, 108–120.

Kadko D. and Butterfield D. A. (1998) The relationship of hydrothermal fluid composition and crustal residence time to maturity of vent fields on the Juan de Fuca Ridge. *Geochim. Cosmochim. Acta* **62**, 1521–1533.

Krabbenhöft A., Eisenhauer A., Böhm F., Vollstaedt H., Fietzke J., Liebetrau V., Augustin N., Peucker-Ehrenbrink B., Müller M. N., Horn C., Hansen B. T., Nolte N. and Wallmann K. (2010) Constraining the marine strontium budget with natural strontium isotope fractionations ($^{87}Sr/^{86}Sr^{*}$, $\delta^{88/86}Sr$) of carbonates, hydrothermal solutions and river waters. *Geochim. Cosmochim. Acta* **74**, 4097–4109.

Li G. and Elderfield H. (2013) Evolution of carbon cycle over the past 100 million years. *Geochim. Cosmochim. Acta* **103**, 11–25.

Luhmann A. J., Tutolo B. M., Bagley B. C., Mildner D. F. R., Scheuermann P. P., Feinberg J. M., Ignatyev K. and Seyfried W. E. (2017a) Chemical and physical changes during seawater flow through intact dunite cores: An experimental study at 150–200 °C. *Geochim. Cosmochim. Acta* **214**, 86–114.

Luhmann A. J., Tutolo B. M., Tan C., Moskowitz B. M., Saar M. O. and Seyfried W. E. (2017b) Whole rock basalt alteration from CO_2-rich brine during flow-through experiments at 150 °C and 150 bar. *Chem. Geol.* **453**, 92–110.

McArthur J. M., Howarth R. J. and Shields G. A. (2012) Strontium isotope stratigraphy. In *The geologic time scale* Elsevier. pp. 127–144.

Menzies M. and Seyfried W. E. Jr. (1979) Basalt-seawater interaction: trace element and strontium isotopic variations in experimentally altered glassy basalt. *Earth Planet. Sci. Lett.* **44**, 463–472.

Mokadem F., Parkinson I. J., Hathorne E. C., Anand P., Allen J. T. and Burton K. W. (2015) High-precision radiogenic strontium isotope measurements of the modern and glacial ocean: Limits on glacial–interglacial variations in continental weathering. *Earth Planet. Sci. Lett.* **415**, 111–120.

Morse J. W. (1978) Dissolution kinetics of calcium carbonate in sea water; VI, The near-equilibrium dissolution kinetics of calcium carbonate-rich deep sea sediments. *Am. J. Sci.* **278**, 344–353.

Morton J. L. and Sleep N. H. (1985) A mid-ocean ridge thermal model: Constraints on the volume of axial hydrothermal heat flux. *J. Geophys. Res. Solid Earth* **90**, 11345–11353.

Mottl M. J. (2003) Partitioning of energy and mass fluxes between mid-ocean ridge axes and flanks at high and low temperature. In *Energy and Mass Transfer in Marine Hydrothermal Systems* (eds. P. E. Halbach, V. Tunnicliffe, and J. R. Hein). Dahlem University Press, Berlin, Germany. pp. 271–286.

Mottl M. J. and Holland H. D. (1978) Chemical exchange during hydrothermal alteration of basalt by seawater—I. Experimental results for major and minor components of seawater. *Geochim. Cosmochim. Acta* **42**, 1103–1115.

Mottl M. J., Holland H. D. and Corr R. F. (1979) Chemical exchange during hydrothermal alteration of basalt by seawater—II. Experimental results for Fe, Mn, and sulfur species. *Geochim. Cosmochim. Acta* **43**, 869–884.

Murray J. W., Leborgnelt R. and Dandonneau Y. (1997) JGOFS studies in the equatorial Pacific. *Deep Sea Res. Part II Top. Stud. Oceanogr.* **44**, 1759–1763.

Nelder J. A. and Mead R. (1965) A simplex method for function minimization. *Comput. J.* **7**, 308–313.

Nielsen S. G., Rehkämper M., Teagle D. A. H., Butterfield D. A., Alt J. C. and Halliday A. N. (2006) Hydrothermal fluid fluxes calculated from the isotopic mass balance of thallium in the ocean crust. *Earth Planet. Sci. Lett.* **251**, 120–133.

Nier A. O. (1938) The isotopic constitution of strontium, barium, bismuth, thallium and mercury. *Phys. Rev.* **54**, 275.

Oelkers E. H. and Gíslason S. R. (2001) The mechanism, rates and consequences of basaltic glass dissolution: I. An experimental study of the dissolution rates of basaltic glass as a function of aqueous Al, Si and oxalic acid concentration at 25 °C and pH= 3 and 11. *Geochim. Cosmochim. Acta* **65**, 3671–3681.

Ogilvie J. F. (1984) A Monte-Carlo approach to error propagation. *Comput. Chem.* **8**, 205–207.

Palmer D. A., Simonson J. M. and Jensen J. P. (2004) Partitioning of electrolytes to steam and their solubilities in steam. In *Aqueous Systems at Elevated Temperatures and Pressures* Academic Press, London. pp. 409–439. Available at: https://www.sciencedirect.com/science/article/pii/B9780125444613500132 [Accessed June 9, 2018].

Palmer M. R. and Edmond J. M. (1989) The strontium isotope budget of the modern ocean. *Earth Planet. Sci. Lett.* **92**, 11–26.

Parkhurst D. L. and Appelo C. A. J. (2013) Description of input and examples for PHREEQC version 3 - A computer program for speciation, batch-reaction, one-dimensional transport, and inverse geochemical calculations. In *U.S. Geological Survey techniques and methods, modeling techniques, groundwater* U.S. Geological Survey, Denver, Colorado.

Pearce C. R., Parkinson I. J., Gaillardet J., Charlier B. L. A., Mokadem F. and Burton K. W. (2015) Reassessing the stable ($\delta^{88/86}$Sr) and radiogenic (^{87}Sr/^{86}Sr) strontium isotopic composition of marine inputs. *Geochim. Cosmochim. Acta* **157**, 125–146.

Pester N. J., Reeves E. P., Rough M. E., Ding K., Seewald J. S. and Seyfried W. E. (2012) Subseafloor phase equilibria in high-temperature hydrothermal fluids of the Lucky Strike Seamount (Mid-Atlantic Ridge, 37°17′N). *Geochim. Cosmochim. Acta* **90**, 303–322.

Scheuermann P. P., Syverson D. D., Higgins J. A., Pester N. J. and Seyfried W. E. (2018) Calcium isotope systematics at hydrothermal conditions: Mid-ocean ridge vent fluids and experiments in the CaSO4-NaCl-H2O system. *Geochim. Cosmochim. Acta* **226**, 18–35.

Seewald J. S. and Seyfried W. E. Jr. (1990) The effect of temperature on metal mobility in subseafloor hydrothermal systems: constraints from basalt alteration experiments. *Earth Planet. Sci. Lett.* **101**, 388–403.

Seyfried W. E. Jr. and Bischoff J. L. (1981) Experimental seawater-basalt interaction at 300°C, 500 bars, chemical exchange, secondary mineral formation and implications for the transport of heavy metals. *Geochim. Cosmochim. Acta* **45**, 135–147.

Seyfried W. E. Jr. and Bischoff J. L. (1977) Hydrothermal transport of heavy metals by seawater: The role of seawater/basalt ratio. *Earth Planet. Sci. Lett.* **34**, 71–77.

Seyfried W. E. Jr. and Bischoff J. L. (1979) Low temperature basalt alteration by sea water: an experimental study at 70 °C and 150 °C. *Geochim. Cosmochim. Acta* **43**, 1937–1947.

Seyfried W. E. Jr. and Mottl M. J. (1982) Hydrothermal alteration of basalt by seawater under seawater-dominated conditions. *Geochim. Cosmochim. Acta* **46**, 985–1002.

Seyfried W. E., Pester N. and Fu Q. (2010) Phase Equilibria Controls on the Chemistry of Vent Fluids from Hydrothermal Systems On Slow Spreading Ridges: Reactivity Of Plagioclase and Olivine Solid Solutions And The Ph-Silica Connection. In *Diversity Of Hydrothermal Systems On Slow Spreading Ocean Ridges* American Geophysical Union (AGU). pp. 297–320. Available at:

https://agupubs.onlinelibrary.wiley.com/doi/abs/10.1029/2009GM000854 [Accessed June 9, 2018].

Shikazono N. and Holland H. D. (1983) The partitioning of strontium between anhydrite and aqueous solutions from 150° to 250 °C. *Econ. Geol. Monogr.* **5**, 320–328.

Simonson J. M. and Palmer D. A. (1993) Liquid-vapor partitioning of HCl(aq) to 350°C. *Geochim. Cosmochim. Acta* **57**, 1–7.

Sleep N. H. (1991) Hydrothermal circulation, anhydrite precipitation, and thermal structure at ridge axes. *J. Geophys. Res. Solid Earth* **96**, 2375–2387.

Staudigel H. (2014) Chemical Fluxes from Hydrothermal Alteration of the Oceanic Crust. In *Treatise on geochemistry* (ed. K. K. Turekian). Elsevier, Oxford, England. pp. 583–606.

Staudigel H., Davies G. R., Hart S. R., Marchant K. M. and Smith B. M. (1995) Large scale isotopic Sr, Nd and O isotopic anatomy of altered oceanic crust: DSDP/ODP sites 417/418. *Earth Planet. Sci. Lett.* **130**, 169–185.

Stein C. A. and Stein S. (1994) Constraints on hydrothermal heat flux through the oceanic lithosphere from global heat flow. *J. Geophys. Res. Solid Earth* **99**, 3081–3095.

Syverson D. D., Scheuermann P., Pester N. J., Higgins J. A. and Seyfried W. E. Jr. (2016) Ca isotope fractionation and Sr/Ca partitioning associated with anhydrite formation at mid-ocean ridge hydrothermal systems: An experimental approach. In *AGU Fall Meeting Abstracts* pp. V51A-3055. Available at: http://adsabs.harvard.edu/abs/2016AGUFM.V51A3055S [Accessed June 9, 2018].

Teagle D. A. H., Alt J. C., Chiba H. and Halliday A. N. (1998a) Dissecting an active hydrothermal deposit: the strontium and oxygen isotopic anatomy of the TAG hydrothermal mound - anhydrite. In *Proceedings of the Ocean Drilling Program, Scientific Results* (eds. P. M. Herzig, S. E. Humphris, D. J. Miller, and R. A. Zierenberg). Ocean Drilling Program, College Station, Texas. pp. 129–142.

Teagle D. A. H., Alt J. C. and Halliday A. N. (1998b) Tracing the chemical evolution of fluids during hydrothermal recharge: Constraints from anhydrite recovered in ODP Hole 504B. *Earth Planet. Sci. Lett.* **155**, 167–182.

Urey H. C. (1947) The thermodynamic properties of isotopic substances. *J. Chem. Soc.*, 562–581.

Vance D., Teagle D. A. H. and Foster G. L. (2009) Variable Quaternary chemical weathering fluxes and imbalances in marine geochemical budgets. *Nature* **458**, 493–496.

Voigt M., Marieni C., Clark D. E., Oelkers E. H. and Gíslason S. R. (in review) Evaluation and refinement of thermodynamic databases for mineral carbonation. *Energy Procedia*.

Vollstaedt H., Eisenhauer A., Wallmann K., Böhm F., Fietzke J., Liebetrau V., Krabbenhöft A., Farkaš J., Tomašovỳch A., Raddatz J. and others (2014) The Phanerozoic $\delta^{88/86}$Sr record of seawater: new constraints on past changes in oceanic carbonate fluxes. *Geochim. Cosmochim. Acta* **128**, 249–265.

976 Wei G., Ma J., Liu Y., Xie L., Lu W., Deng W., Ren Z., Zeng T. and Yang Y. (2013)
977 Seasonal changes in the radiogenic and stable strontium isotopic composition of
978 Xijiang River water: Implications for chemical weathering. *Chem. Geol.* **343**, 67–75.

979 Young E. D., Galy A. and Nagahara H. (2002) Kinetic and equilibrium mass-dependent
980 isotope fractionation laws in nature and their geochemical and cosmochemical
981 significance. *Geochim. Cosmochim. Acta* **66**, 1095–1104.

982 Ypma T. (1995) Historical Development of the Newton–Raphson Method. *SIAM Rev.* **37**,
983 531–551.

984

985 Appendix A Model details

986 The rate of anhydrite precipitation is constrained using the relationship

$$\frac{\mathrm{d}m_{\mathrm{Anhydrite}}}{\mathrm{d}m_{\mathrm{Basalt}}} = k(\Omega_{\mathrm{Anhydrite}} - 1) \tag{A.1}$$

987 where $\Omega_{\mathrm{Anhydrite}}$ stands for the saturation state of the liquid with respect to anhydrite, and k is
988 a fitted constant. This corresponds to a simple form of the empirical rate law (Morse, 1978)
989 assuming that $\mathrm{d}m_{\mathrm{Basalt}}/\mathrm{d}t$ does not vary significantly with liquid composition and that basalt
990 dissolution and anhydrite precipitation have the same relative dependency on temperature
991 during the short initial heating period. The anhydrite saturation state is calculated from the
992 aqueous solution composition using PHREEQC; for this calculation, the aqueous solution
993 composition other than Ca, Sr, and SO_4^{2-} is estimated by a linear mixture between the known
994 initial seawater composition and first sample compositions as function of m_{Basalt}.

995 The amount of Sr incorporated into anhydrite is calculated using the partition
996 coefficient

$$D_{\mathrm{Sr}} = \frac{\mathrm{d}m^{\mathrm{Sr}}_{\mathrm{Anhydrite}}/\mathrm{d}m^{\mathrm{Ca}}_{\mathrm{Anhydrite}}}{m^{\mathrm{Sr}}_{\mathrm{Liquid}}/m^{\mathrm{Ca}}_{\mathrm{Liquid}}} \tag{A.2}$$

997 with m_p^i denoting the mass of element i in phase p. Its value is determined by finding the best
998 fit to the boundary values (as for k), and both of these parameters are allowed to differ for the
999 individual experiments to account for the different reaction kinetics and temperatures.

1000 The evolution of the Sr isotopic composition is modelled using the two fractionation
1001 factors between anhydrite and liquid and during non-stoichiometric basalt dissolution. The
1002 values for both fractionation factors are estimated by fitting the model to the boundary values,
1003 assuming distinct $\alpha^{88/86}_{\text{CrystBasalt-Liquid}}$ for the two temperatures used. Aqueous $^{87}Sr/^{86}Sr$ is
1004 calculated from the stable Sr isotope ratios by re-normalisation to a $^{86}Sr/^{88}Sr$ value of 0.1194
1005 using the exponential fractionation law.

1006 In addition to the isotopic fractionation factors, the rate of anhydrite precipitation and
1007 the bulk Sr partition coefficient D_{Sr}, the following relationships define the evolution of the Sr
1008 isotope ratios in the liquid. For each isotope of ^{A}Sr with mass number A,

$$\frac{\mathrm{d}m^{\,^{A}\mathrm{Sr}}_{\text{Liquid}}}{\mathrm{d}m_{\text{Basalt}}} = c^{\,^{A}\mathrm{Sr}}_{\text{Anhydrite}} \frac{\mathrm{d}m_{\text{Anhydrite}}}{\mathrm{d}m_{\text{Basalt}}} + c^{\,^{A}\mathrm{Sr}}_{\text{Basalt}} \tag{A.3}$$

1009 where m_p^i and c_p^i denote the mass and concentration of i in phase p. Furthermore, basic mass
1010 balance implies $\sum_A m_p^{\,^{A}\mathrm{Sr}} = m_p^{\mathrm{Sr}}$ and $\sum_A c_p^{\,^{A}\mathrm{Sr}} = c_p^{\mathrm{Sr}}$. Due to its negligible abundances, ^{84}Sr
1011 was ignored in the model calculations. Based on a given $\alpha^{88/86}$, the $\alpha^{87/86}$ in the model is
1012 calculated according to the kinetic mass fractionation law (Young et al., 2002)

$$\alpha^{A/86} = \left(\alpha^{B/86}\right)^{\beta} \tag{A.4}$$

1013 where β is defined as

$$\beta = \frac{\ln \dfrac{M_{\,^{A}\mathrm{Sr}}}{M_{\,^{86}\mathrm{Sr}}}}{\ln \dfrac{M_{\,^{B}\mathrm{Sr}}}{M_{\,^{86}\mathrm{Sr}}}} \tag{A.5}$$

1014 where $M_{\,^{X}\mathrm{Sr}}$ denotes the atomic mass of isotope ^{X}Sr. The kinetic mass fractionation equation
1015 was chosen as opposed to the equilibrium mass fractionation equation due to the relatively
1016 fast Sr precipitation rates. However, due to the negligible difference of the β values in both
1017 equations, this does not significantly impact the results.

The solutions to the differential equation system are computed numerically using the NDSolve function of Wolfram Mathematica in combination with the IPhreeqc modules (Charlton and Parkhurst, 2011), essentially taking a sequence of steps in the independent variable m_{Basalt} starting at the initial values, and using an adaptive procedure to determine the size of the steps depending on the variation of the solution in a particular region. The values for the model parameters (k, D_{Sr} and the different $\alpha^{88/86}$) are found by numerically minimising the sum of squared errors between the model predictions and the first sample composition, weighted by the reciprocal of the variance and using the Nelder-Mead method (Nelder and Mead, 1965) implementation in Wolfram Mathematica.

Tables

Table 1: Experimental parameters of the basalt-seawater experiments.

			Starting materials / g		
Experiment	T / °C	Basalt type	Seawater	Basalt	Duration / days
BSW04	250	Glassy	275.0	27.50	53
BSW05	250	Crystalline	275.0	27.50	53
BSW06	290	Glassy	220.0	22.01	92
BSW07	290	Crystalline	220.0	22.00	93

Table 2: Composition (wt. %) of the basaltic glass and crystalline basalt used as starting materials.

Sample	SiO_2	Al_2O_3	Fe_2O_3[c]	MgO	CaO	Na_2O	K_2O	TiO_2	MnO	P_2O_5	Total
Glass[a]	48.1	14.6	12.0	9.1	11.8	2.0	0.3	1.6	0.2	0.2	99.9
Crystalline[b]	47.9	13.4	12.3	10.0	12.2	1.5	0.3	1.6	0.2	0.2	99.1

[a] From Oelkers and Gislason (2001)
[b] From Gudbrandsson et al. (2011)
[c] Most iron is Fe^{2+}

Table 3: Sr content and isotopic composition of the basalt powders used as reactants in the experiments. The uncertainties are the 95 % confidence intervals (≈ 1.96 standard errors).

	Basaltic glass	Crystalline basalt
Sr / ppm	138 ± 20	126 ± 20
$^{87}Sr/^{86}Sr$	0.7031929 ± 0.0000028	0.7031887 ± 0.0000026
$\delta^{88/86}Sr$	0.2304 ± 0.0075	0.2592 ± 0.0075

Table 4: Chemical compositions of the seawater used as reactant and of the liquid samples taken during the experiments. Rows labelled "Quenched" show compositions of the liquid in the reactor after terminating the experiment by quenching. The uncertainties (±) designate the 95 % confidence interval (~2 standard errors), while '< LOD' indicates values that were below the detection limits (listed below the table). Uncertainties for all data are provided in Electronic Supplementary Table 1.

Experiment	Sample	Duration / days	pH	Fluid mass / g	Concentration / mmol/kg									$^{87}Sr/^{86}Sr$		$\delta^{88}Sr$ / ‰	
					Na	Mg	Si	K	Ca	Sr	Fe	Cl	SO_4^{2-}	Value	± / ppm	Value	±
	Seawater		8.14		474	55	< LOD	11.8	10.3	0.0896	0.040	597.4	29.05	0.7091729	2.8	0.372	0.007
BSW04 250 °C basaltic glass	BSW04-01	1.0	7.71	275	489	17.0	14.4	12.9	16.8	0.0210	0.27	599.9	0.6039	0.7034758	2.7	0.214	0.007
	BSW04-02	3.8	8.72	257	491	0.56	13.8	13.6	35.8	0.0435	0.0069	606.5	0.3053	0.7034811	2.5	0.248	0.006
	BSW04-03	6.8	9.09	235	493	0.106	13.4	13.7	39.7	0.0497	0.0008	619.0	0.2867	0.7035802	2.6	0.273	0.006
	BSW04-04	13.9	9.48	212	500	< LOD	10.5	13.8	43.6	0.0633	< LOD	620.4	0.2951	0.7043252	2.8	0.280	0.007
	BSW04-05	21.0	9.58	190	504	< LOD	9.8	13.8	45.8	0.0737	< LOD	624.5	0.2893	0.7048168	2.8	0.311	0.007
	BSW04-06	33.9	9.65	169	575	< LOD	9.2	15.9	42.8	0.0566	< LOD	684.6	0.3454	0.7045957	2.7	0.289	0.008
	BSW04-07	52.9	9.52	148	601	< LOD	10.5	16.9	36.9	0.0593	< LOD	704.1	0.3501	0.7042755	2.6	0.298	0.006
	Quenched				513	< LOD	4.25	9.6	46.9	0.0433	< LOD	621.9	4.003				
BSW05 250 °C crystalline basalt	BSW05-01	1.0	3.74	275	484	46.7	18.2	14.7	1.28	0.0074	1.37	608.0	14.854	0.7074845	2.7	0.194	0.006
	BSW05-02	3.8	4.01	254	479	42.9	20.4	15.2	1.43	0.0066	2.0	603.8	12.448	0.7075882	3.0	0.225	0.007
	BSW05-03	6.8	4.83	232	490	40.4	20.6	15.8	1.63	0.0098	2.4	610.8	10.150	0.7083240	2.6	0.254	0.006
	BSW05-04	14.0	5.89	212	480	20.9	17.1	16.1	10.3	0.0196	1.43	597.5	0.9019	0.7062790	2.7	0.158	0.007
	BSW05-05	21.0	9.03	192	489	0.84	6.0	16.7	35.7	0.0678	0.014	608.3	0.2906	0.7042098	2.7	0.168	0.007
	BSW05-06	33.9	9.01	172	494	0.31	10.4	16.7	37.7	0.0779	0.007	620.1	0.2631	0.7044848	2.7	0.165	0.007
	BSW05-07	52.9	9.08	151	502	0.172	9.9	17.1	40.6	0.0926	0.004	628.9	0.2544	0.7048623	2.7	0.189	0.007
	Quenched				482	< LOD	3.97	16.1	44.5	0.0982	< LOD	622.0	4.003				

Detection limits (LOD) in mmol/kg were approximately: Mg: 0.026; Si: 0.018; Fe (BSW04 and BSW05): 0.0001; Fe (BSW06 and BSW07): 0.02

1044 **Table 4**: (continued)

Experiment	Sample	Duration / days	pH	Fluid mass / g	Concentration / mmol/kg									$^{87}Sr/^{86}Sr$		$\delta^{88}Sr$ / ‰	
					Na	Mg	Si	K	Ca	Sr	Fe	Cl	SO_4^{2-}	Value	± / ppm	Value	±
BSW06 290 °C basaltic glass	BSW06-01	0.8	8.36	220	524	6.9	23.7	12.0	28.6	0.0342	< LOD	636.5	0.181	0.7034329	2.5	0.234	0.006
	BSW06-02	3.0	9.20	200	541	0.078	19.7	12.3	42.4	0.0496	< LOD	643.5	0.124	0.7034302	2.9	0.261	0.011
	BSW06-03	7.9	9.40	180	545	0.0154	13.5	12.6	45.4	0.0539	< LOD	654.6	0.120	0.7035378	2.6	0.278	0.006
	BSW06-04	16.0	9.41	160	550	0.0080	15.7	13.5	46.3	0.0611	< LOD	667.1	0.123	0.7036699	2.8	0.273	0.006
	BSW06-05	33.8	9.50	141	561	0.0062	13.9	14.2	44.9	0.0674	< LOD	689.6	0.122	0.7038923	2.5	0.286	0.006
	BSW06-06	54.9	9.56	122	582	0.0105	12.4	18.9	62.4	0.1114	< LOD	736.3	0.141	0.7038094	2.5	0.276	0.006
	BSW06-07	92.0	9.50	104	608	0.0200	10.6	23.9	78.8	0.1706	< LOD	806.6	0.132	0.7041144	2.6	0.260	0.006
BSW07 290 °C crystalline basalt	BSW07-01	0.9	4.93	219	512	30.6	25.8	14.3	2.25	0.0025	4.7	631.3	3.951	0.7040288	4.1	-0.057	0.009
	BSW07-02	3.8	8.40	201	516	5.0	9.8	15.5	29.9	0.0369	0.50	648.0	0.175	0.7035317	2.9	0.082	0.007
	BSW07-03	8.7	8.92	183	515	0.55	14.6	15.6	38.0	0.0556	0.044	656.7	0.132	0.7036126	2.7	0.125	0.007
	BSW07-04	16.9	9.01	165	511	0.41	15.6	15.8	39.3	0.0619	0.033	660.2	0.124	0.7038432	2.9	0.121	0.007
	BSW07-05	34.6	9.03	148	528	0.29	16.6	16.4	41.7	0.0742	0.032	678.0	0.062	0.7043048	2.6	0.162	0.006
	BSW07-06	55.7	9.13	128	543	0.201	16.3	17.0	43.8	0.0903	< LOD	700.5	0.057	0.7047286	2.9	0.202	0.007
	BSW07-07	92.8	9.22	110	589	0.127	14.8	18.4	48.6	0.1124	< LOD	754.2	0.113	0.7051157	2.6	0.195	0.006

Figures

Fig. 1: Schematic design of Ti-autoclaves used for the experiments in this study. The Ti-autoclaves are rocked to ensure mixing of the solids with the seawater. The cooling apparatus attached to a valve allows fluid samples to be taken during the experimental run.

Fig. 2: Scanning electron microscopy images of the starting basalt powders used in the 250 °C experiments (a, b) and of the solid alteration products recovered from experiments BSW04 and BSW05 (c-f).

Fig. 3: Aqueous concentrations of Ca, Mg, SO_4^{2-}, Na, Cl, Fe, and Si as well as pH of seawater reacting with basaltic glass (solid lines) and crystalline basalt (dashed lines) at 250 °C. The errors bars show the 95 % confidence intervals (~2 standard errors), which are smaller than the symbol size where no error bars are shown. Initial Si concentrations (below the detection limit) are shown as zero.

Fig. 4: Fluid sample composition of experiments with basaltic glass and crystalline basalt at 290 °C (cf. Fig. 3).

Fig. 5: Strontium concentration, radiogenic $^{87}Sr/^{86}Sr$ and stable $\delta^{88/86}Sr$ isotope ratios of seawater reacting with basaltic glass and crystalline at temperatures of 250 °C (left side) and 290 °C (right side). The dashed lines show the isotopic composition of the basalt used in the experiments. The 95 % confidence intervals (~2 standard errors) for all values are smaller than the symbol size.

Fig. 6: Evolution of aqueous Mg and Ca concentrations during the experiments in comparison with similar experiments of Seyfried and Bischoff (1979; 1981) conducted at temperatures of 150 °C and 300 °C.

Fig. 7: Model predictions (dashed curves) of anhydrite precipitation as well as aqueous Sr concentrations, $^{87}Sr/^{86}Sr$ ratios and stable $\delta^{88/86}Sr$ values plotted as a function of basalt dissolution during the first 24 h. The symbols show the initial seawater and first sample compositions, and the errors bars and shaded areas show the 95 % confidence intervals, which are smaller than the symbol size where no error bars are shown. For the crystalline experiment at 250 °C, the $\delta^{88/86}Sr$ model evolution between 7 and 14 days is shown as well.

Fig. 8: Model predictions (dashed curves) of aqueous Sr concentrations and $^{87}Sr/^{86}Sr$ during the first 24 hours for the 250 °C and 290 °C experiments. The symbols connected by solid lines show the later evolution of the liquids. The grey arrows and labels show the processes leading to the changes in the two parameters during the basalt-fluid reactions. Errors bars and shaded areas show the 95 % confidence intervals, which are smaller than the symbol size where no error bars are shown.

Fig. 9: Plot of best-fit fractionation factors $\varepsilon^{88/86}_{\text{Anhydrite-Liquid}}$ vs. $\varepsilon^{88/86}_{\text{CrystBasalt-Liquid}}$ (fractionation during non-stoichiometric dissolution of crystalline basalt at (a) 250 °C and (b) 290 °C). The blue point shows the maximum likelihood value while the shaded region is the 95 % confidence interval. Note the different scale of $\varepsilon^{88/86}_{\text{CrystBasalt-Liquid}}$ in (a) and (b).

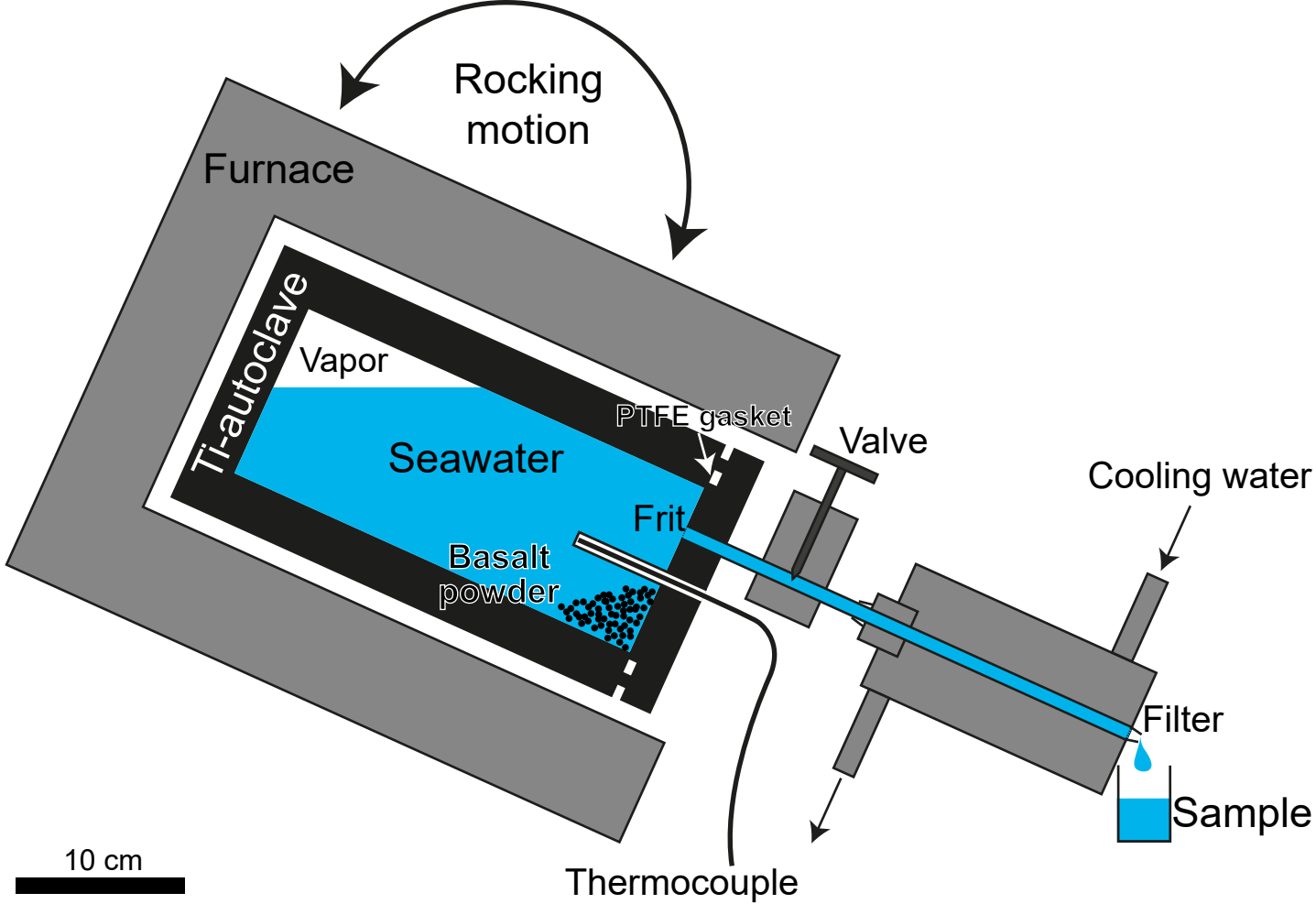
Rocking
motion
Furnace
Ti-autoclave
Vapor
Seawater
PTFE gasket
Valve
Cooling water
Frit
Basalt
powder
Filter
Sample
10 cm
Thermocouple

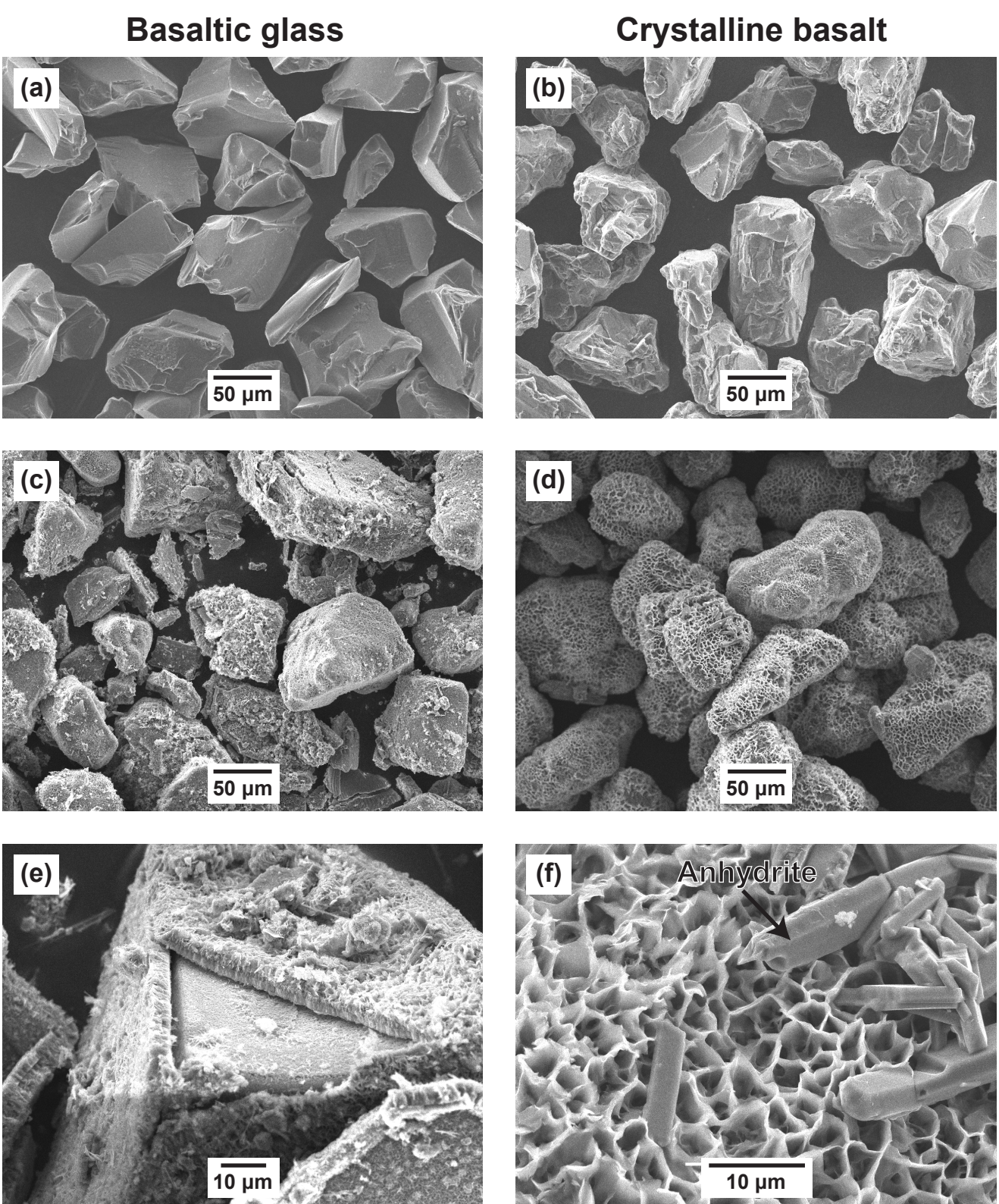
Basaltic glass
Crystalline basalt
(a)
50 µm
(b)
50 µm
(c)
50 µm
(d)
50 µm
(e)
10 µm
(f)
Anhydrite
10 µm

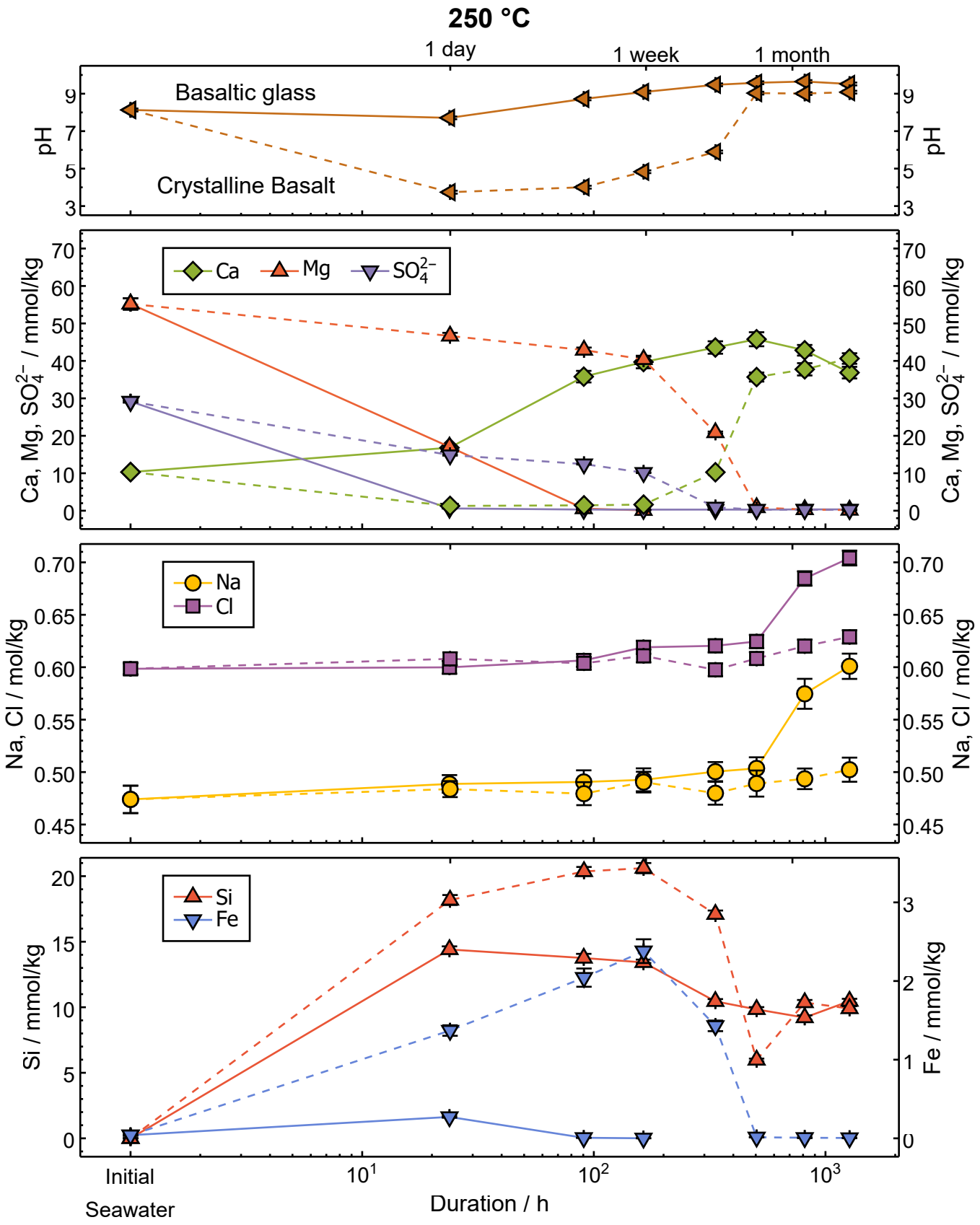
250 °C
1 day
1 week
1 month
Basaltic glass
Crystalline Basalt
pH
Ca
Mg
SO_4^{2-}
Ca, Mg, SO_4^{2-} / mmol/kg
Na
Cl
Na, Cl / mol/kg
Si
Fe
Si / mmol/kg
Fe / mmol/kg
Initial
Seawater
10^1
10^2
10^3
Duration / h

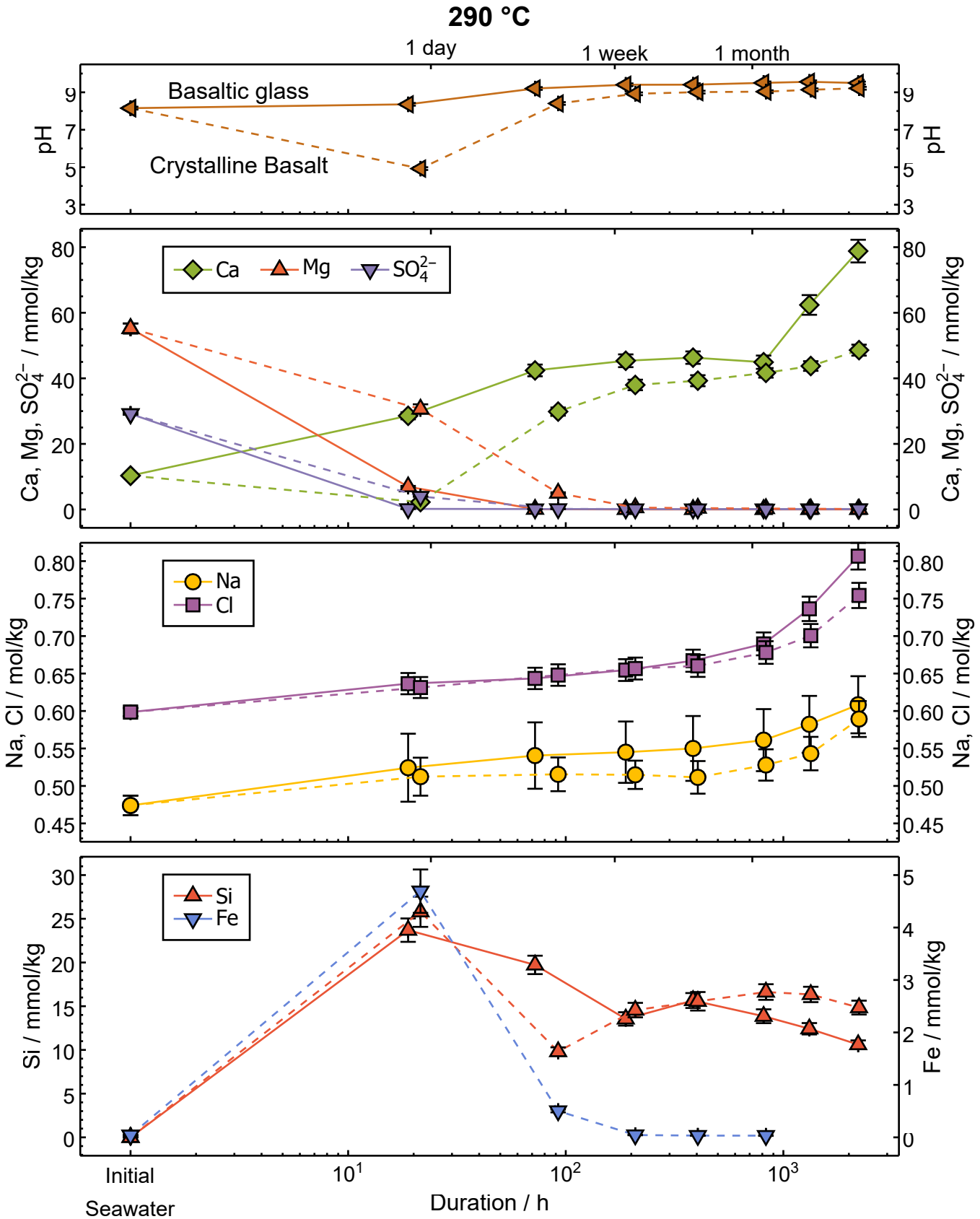
290 °C
1 day
1 week
1 month
Basaltic glass
Crystalline Basalt
pH
Ca
Mg
SO_4^{2-}
Ca, Mg, SO_4^{2-} / mmol/kg
Na
Cl
Na, Cl / mol/kg
Si
Fe
Si / mmol/kg
Fe / mmol/kg
Initial
Seawater
Duration / h

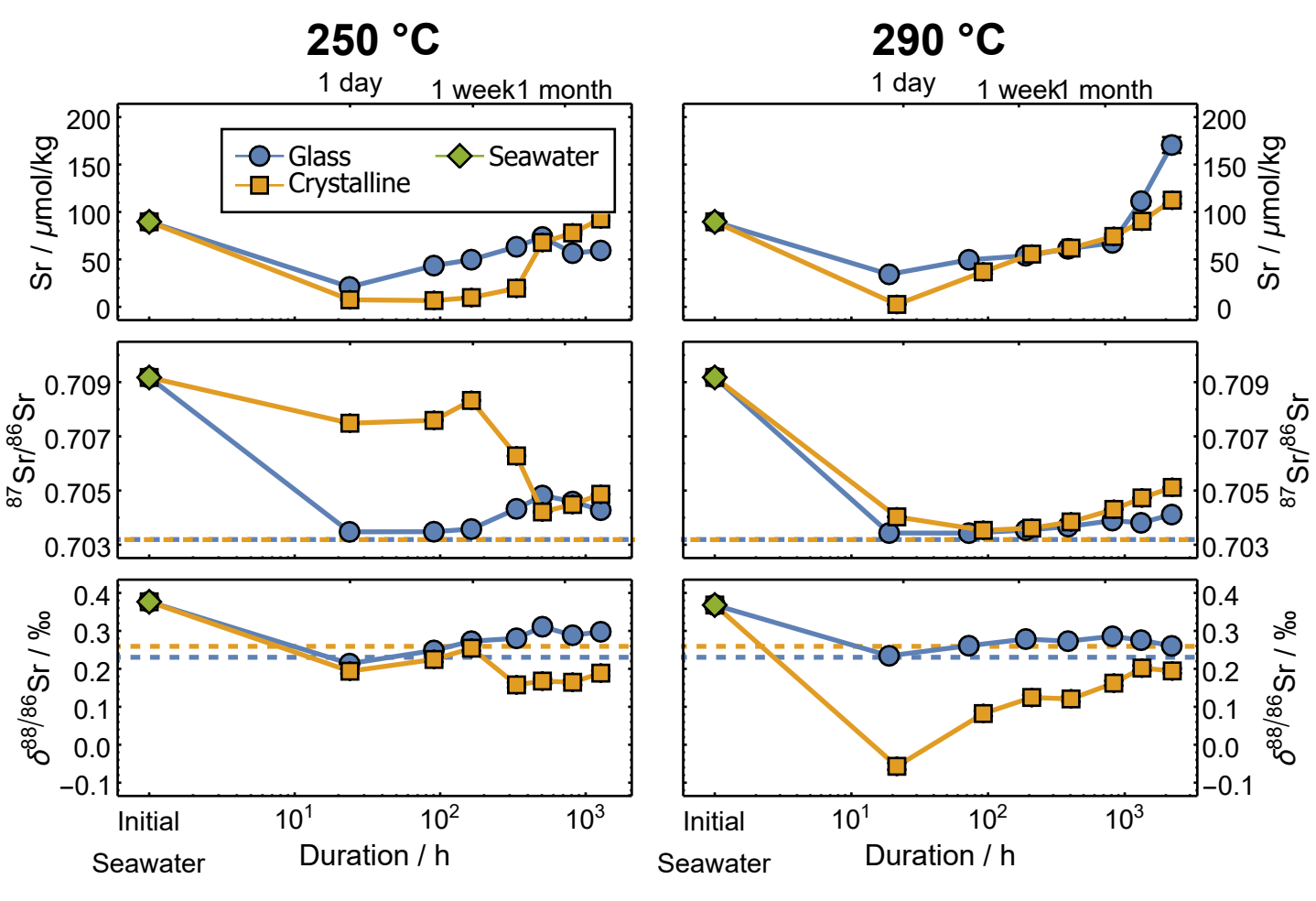
250 °C
290 °C
1 day
1 week
1 month
Glass
Crystalline
Seawater
Sr / μmol/kg
87Sr/86Sr
δ88/86Sr / ‰
Initial
Seawater
Duration / h

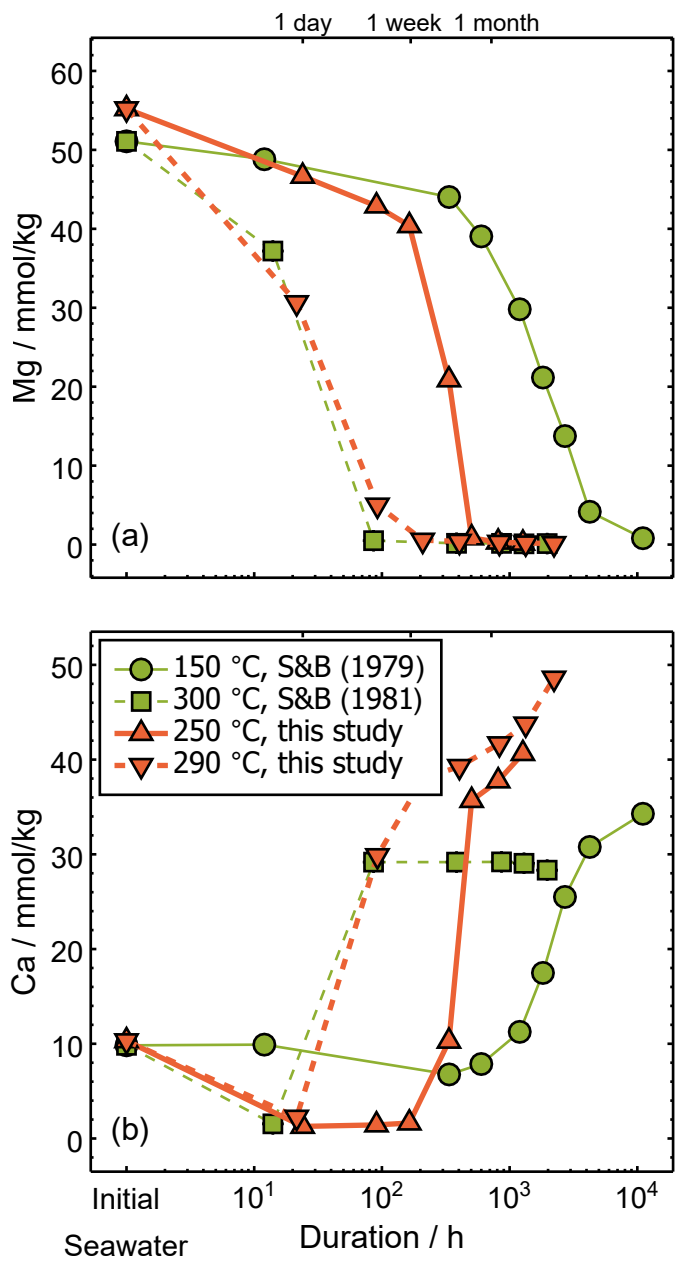
1 day
1 week
1 month
Mg / mmol/kg
(a)
Ca / mmol/kg
150 °C, S&B (1979)
300 °C, S&B (1981)
250 °C, this study
290 °C, this study
(b)
Initial Seawater
Duration / h

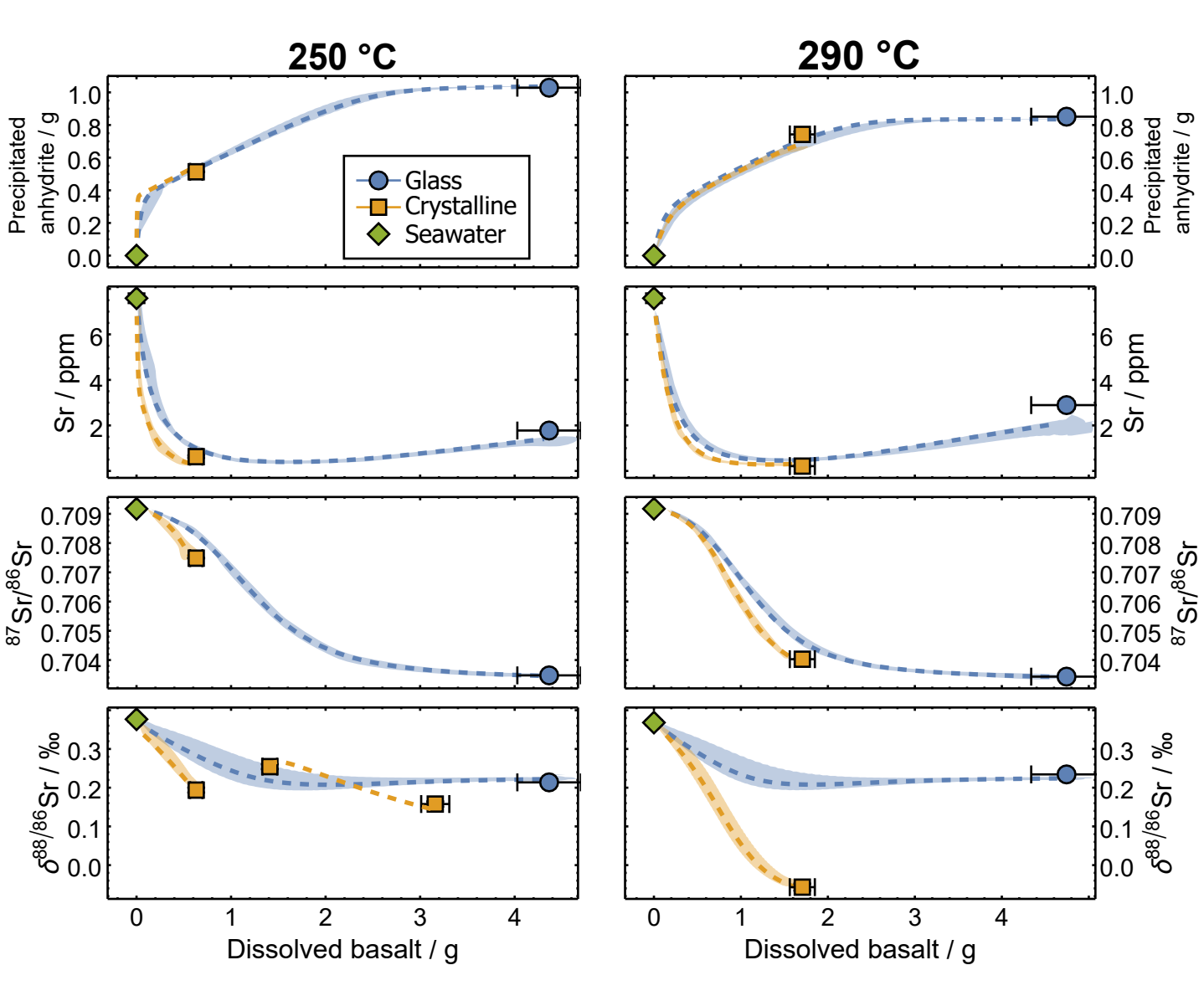
250 °C
290 °C
Precipitated anhydrite / g
Glass
Crystalline
Seawater
Sr / ppm
$^{87}Sr/^{86}Sr$
$\delta^{88/86}Sr$ / ‰
Dissolved basalt / g

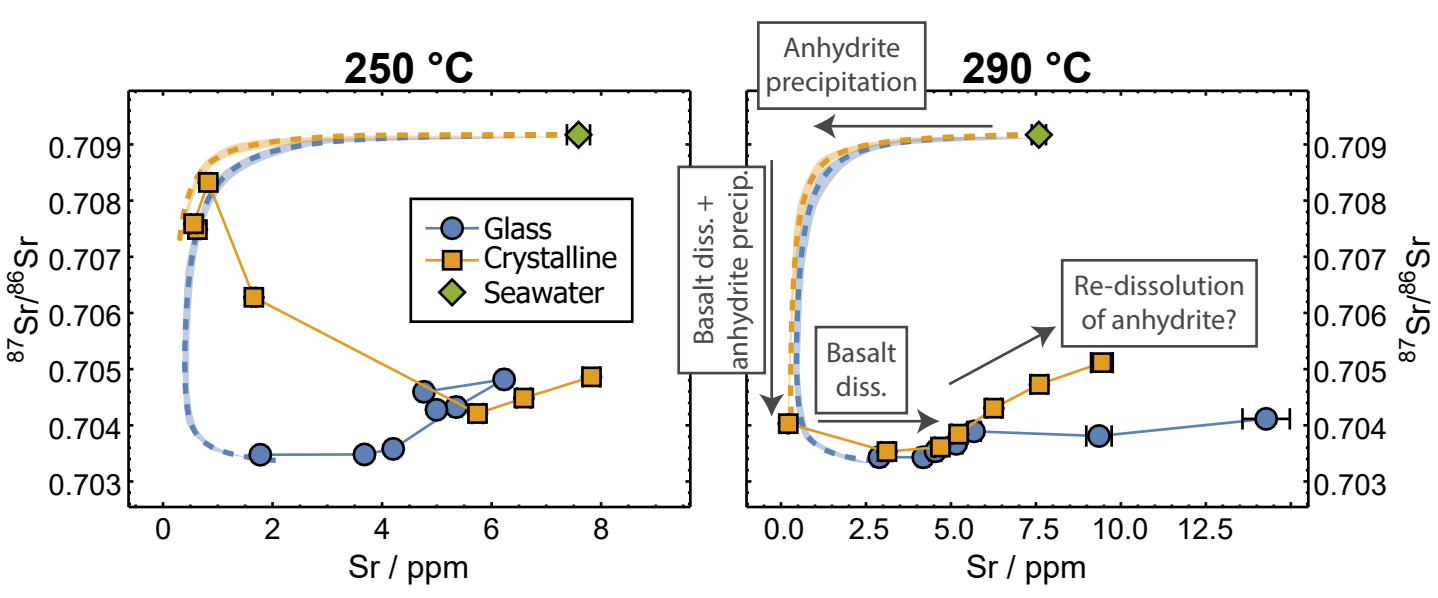
250 °C
290 °C
Anhydrite precipitation
Basalt diss. + anhydrite precip.
Basalt diss.
Re-dissolution of anhydrite?
Glass
Crystalline
Seawater
$^{87}Sr/^{86}Sr$
Sr / ppm
0.709
0.708
0.707
0.706
0.705
0.704
0.703
0
2
4
6
8
0.0
2.5
5.0
7.5
10.0
12.5

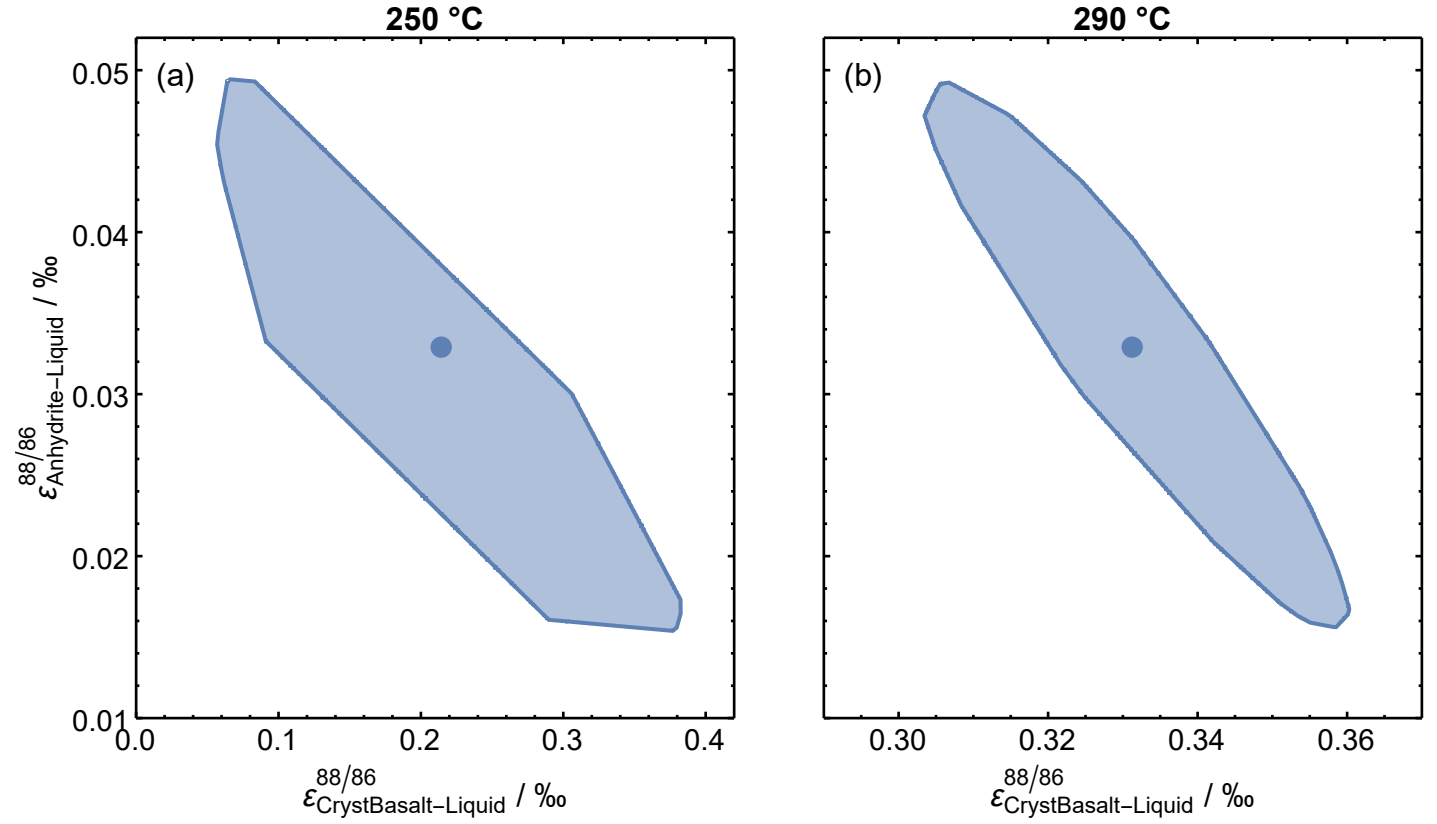
250 °C
290 °C
(a)
(b)
0.05
0.04
0.03
0.02
0.01
0.0
0.1
0.2
0.3
0.4
0.30
0.32
0.34
0.36
$\varepsilon^{88/86}_{\text{Anhydrite–Liquid}}$ / ‰
$\varepsilon^{88/86}_{\text{CrystBasalt–Liquid}}$ / ‰
$\varepsilon^{88/86}_{\text{CrystBasalt–Liquid}}$ / ‰

Note the presence of amorphous phases in all samples. The *hkl*-reflections correspond mainly to ferrous saponite. Zincite (20 wt.%; grey bars) was used as an internal standard.

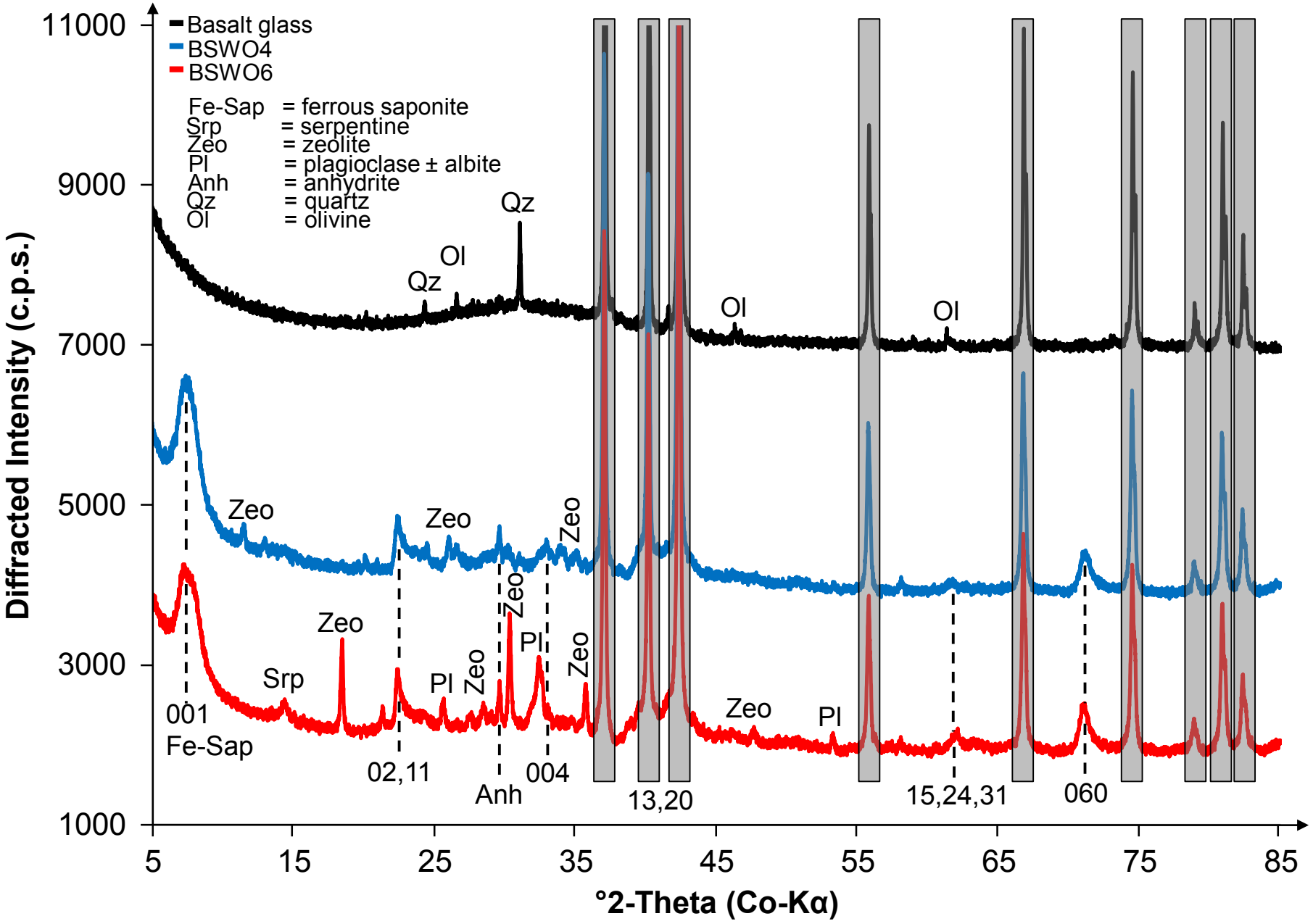

Note the absence of amorphous phases in all samples. The *hkl*-reflections correspond to ferrous saponite. Zincite (20 wt.%; grey bars) was used as an internal standard.

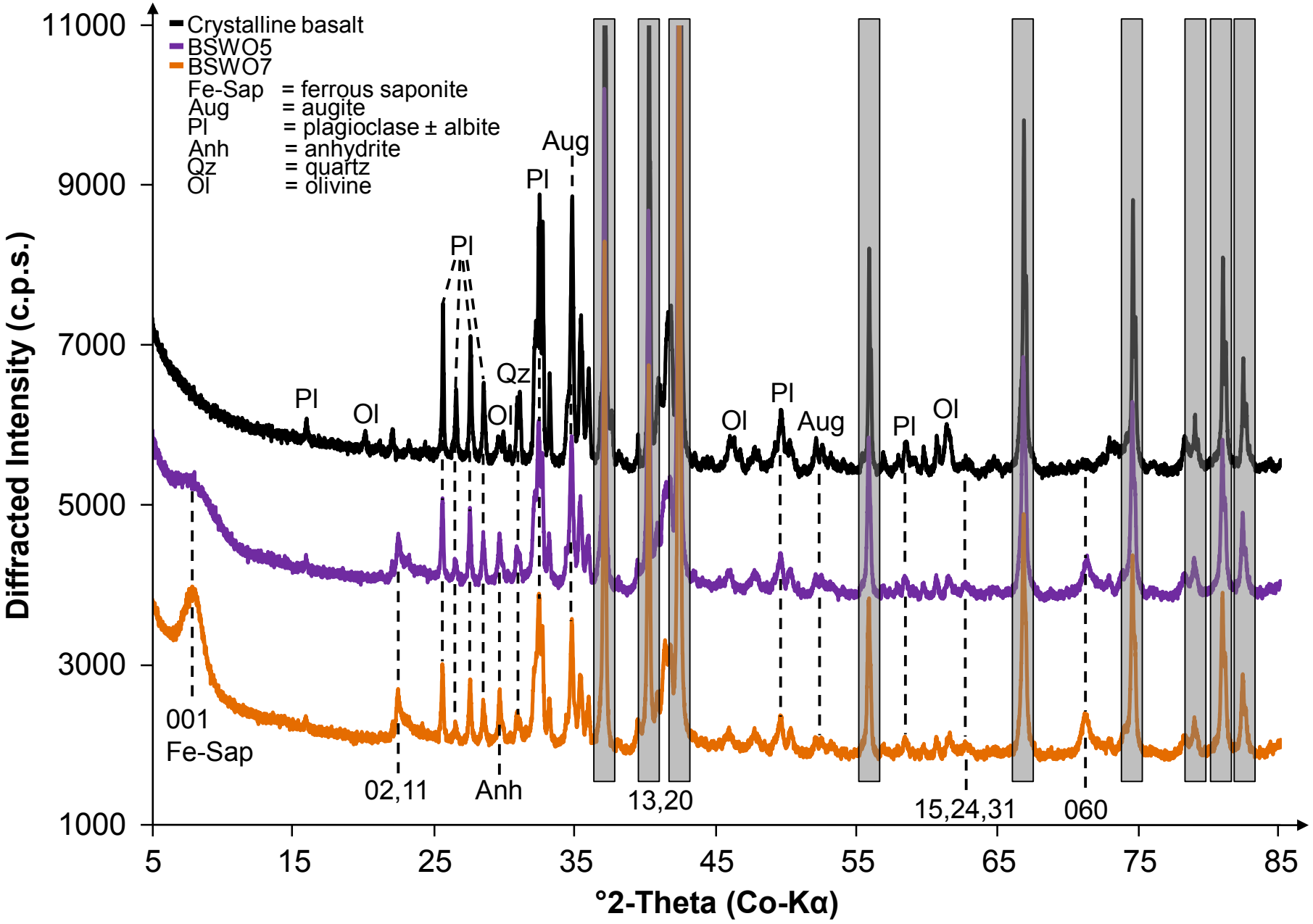

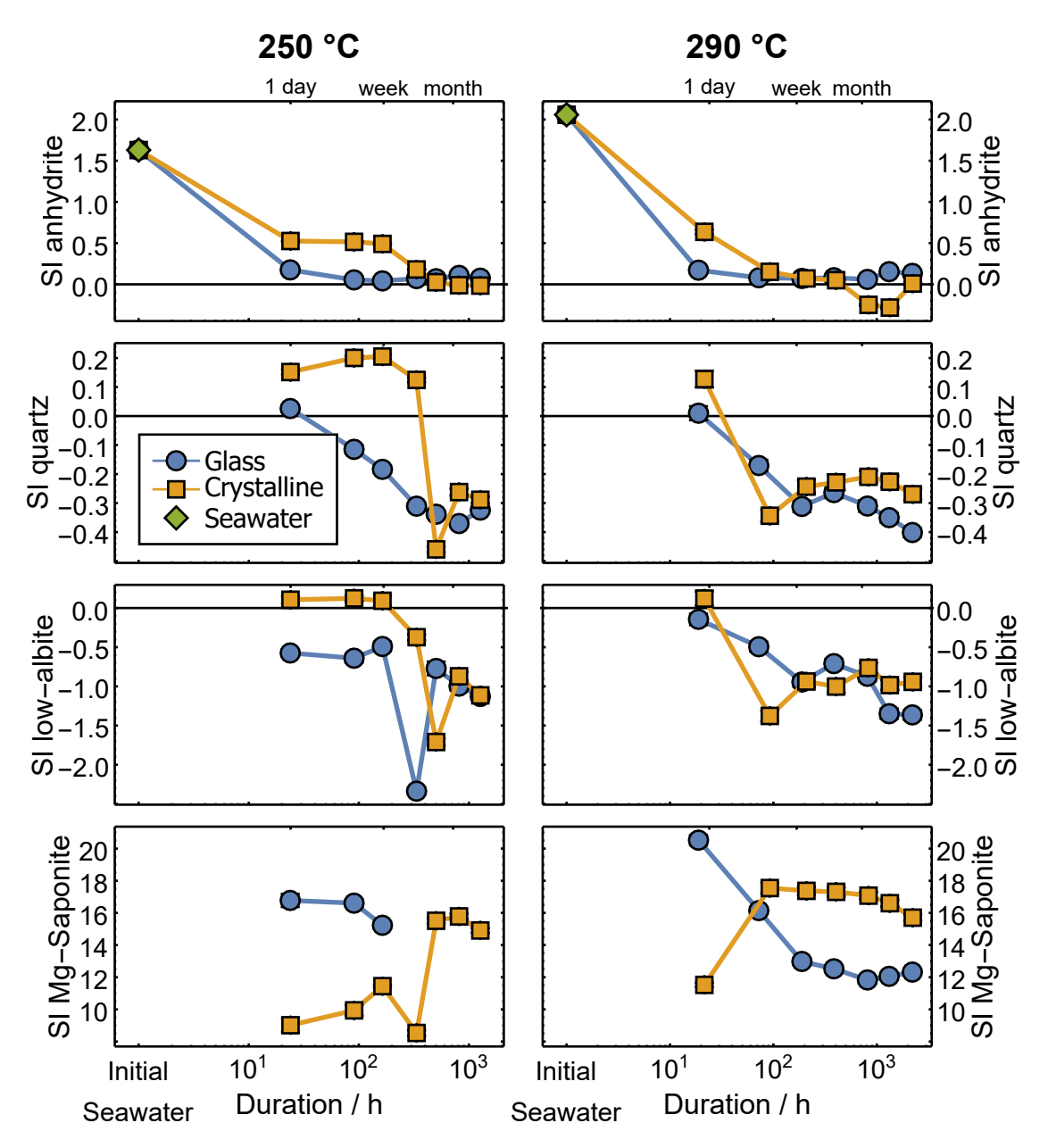
250 °C
290 °C
1 day
week
month
SI anhydrite
SI quartz
SI low−albite
SI Mg−Saponite
Glass
Crystalline
Seawater
Initial
Seawater
Duration / h